

Wind Power Plant North Sea - Wind Farm Interaction

The effect of wind farming on mesoscale flow

A.J. Brand

ECN-E--09-041



Acknowledgement/Preface

This work was performed in the framework of the Dutch Ministry of Economic Affairs BSIK programme We@Sea, project "Windenergiecentrale Noordzee - Parkinteractie" (We@Sea/BSIK 2005/002).

Measured data by courtesy of L.E. Jensen of Dong Energy A/S as prepared by K.S. Hansen in the framework of the European UPWIND research project under contract with the European Commission (CE Contract Number 019945 (SES6)).

Abstract

This report is the final report of the project "Wind power plant North Sea - Wind Farm Interaction" (Windenergiecentrale Noordzee - Parkinteractie; We-at-Sea / BSIK 2005/002; ECN 79446.01.01).

In this project a new method has been developed for determining the interaction between a wind farm and the prevailing wind. In addition first insights on the impact of a wind farm on the downstream wind have been presented.

Contents

List of tables	4
1. Introduction	7
2. Prior work	9
3. Flow model	11
3.1 Overview of the flow modeling approach	11
3.2 Definition of the flow problem	11
3.3 Governing equations	13
3.3.1 Dimensional form	13
3.3.2 Non-dimensional form	19
3.4 Momentum equations	20
3.4.1 Discretization	20
3.4.2 Representation	21
3.4.3 Solution procedure	22
3.4.4 Formal order of the numerical scheme	22
3.4.5 Numerical stability	25
3.4.6 Conservation of mass and energy	26
3.5 Continuity equation revisited	28
3.5.1 Lagrange multiplier method	28
3.5.2 Representation	29
3.5.3 Solution procedure	30
3.6 Turbulence parameterization	31
3.7 Wind turbine parameterization	32
3.8 Initial and boundary conditions	33
3.8.1 Boundary conditions	33
3.8.2 Initial conditions	34
3.9 Estimate of discretization error	35
3.10 Translation from grid-cell averaged velocity to point velocity	36
4. Validation	39
5. Predictions	43
5.1 Overview of predictions	43
5.2 Resolved velocity profiles	43
5.2.1 Empty set	43
5.2.2 Wind turbine	43
5.2.3 Wind farm	43
5.3 Impact of wind farm design parameters and meteorological parameters	48
6. Summary	49
References	51

List of tables

Table 3.1	<i>Scales in the planetary boundary layer with wind farming</i>	14
Table 3.2	<i>Scale analysis of the continuity equation</i>	16
Table 3.3	<i>Scale analysis of the momentum equation</i>	16
Table 3.4	<i>Scale analysis of the turbulent fluxes</i>	19
Table 3.5	<i>Coefficients in the modified Baldwin-Lomax model</i>	32
Table 3.6	<i>Dutton-Panofsky parameter according to Dyrbye and Hansen</i>	32
Table 3.7	<i>Order p and error ε of the scheme in vertical direction at three vertical positions</i>	36
Table 3.8	<i>Order p and error ε of the scheme in horizontal direction at three vertical positions</i>	36
Table 4.1	<i>Point values of the exponent m of the streamwise velocity deficit decay and the initial velocity deficit ΔU_{ini}</i>	41
Table 4.2	<i>Velocity recovery distance d_{VR} and the minimum save distance d_{MS}, as calculated from the data in table 4.1</i>	41

List of figures

Figure 3.1	<i>Velocity decomposition</i>	12
Figure 3.2	<i>Vertical (left) and horizontal (right) length scales</i>	15
Figure 3.3	<i>Length and velocity scales in the planetary boundary layer with wind farming</i>	15
Figure 3.4	<i>Minimal horizontal grid spacing for different combination of the geostrophic height and the surface roughness length</i>	27
Figure 3.5	<i>Optimal solution of the flow problem</i>	28
Figure 3.6	<i>Initial profiles of streamwise velocity u, spanwise velocity v and turbulent viscosity k_m</i>	34
Figure 3.7	<i>Horizontal lay-out of the grid cells in relation to the horizontal area covered by the wind farm, and definition sketch of distances and length scales</i>	37
Figure 3.8	<i>Illustration of the concepts of initial velocity deficit and streamwise velocity recovery distance</i>	38
Figure 4.1	<i>Velocity W relative to the upstream velocity W_{ups} as a function of distance d_x downstream the Horns Rev wind farm</i>	40
Figure 4.2	<i>Velocity W relative to the upstream velocity W_{ups} as a function of distance d_x downstream the Nysted wind farm</i>	41
Figure 5.1	<i>Vertical profiles of streamwise velocity u and spanwise velocity v in the four corners of the numerical domain for a geostrophic height of 500 m and a surface roughness length of 0.1 mm</i>	44
Figure 5.2	<i>Like figure 5.1 but for a geostrophic height of 1500 m</i>	44
Figure 5.3	<i>Like figure 5.1 but for a surface roughness length of 1 cm</i>	45
Figure 5.4	<i>Vertical profiles of streamwise velocity u and spanwise velocity v for different distances d_x behind a wind turbine</i>	46
Figure 5.5	<i>Like figure 5.4 but for a wind farm</i>	46
Figure 5.6	<i>Impact of nominal power density P_{nom}/A_{farm} for a wind farm operating in a geostrophic velocity of 14 m/s</i>	47
Figure 5.7	<i>Impact of geostrophic velocity G on a wind farm with a nominal power density of 5 MW/km²</i>	47

Summary

Motivation

Over the years offshore wind farms tend to be placed closer together, as already illustrated by OWEZ and Princess Amalia Wind Farm (separated 15 km) in the Netherlands or Horns Rev I and II (separated 23 km) in Denmark. Since these separation distances are between 5 and 10 times the wind farm's horizontal scale, the velocity deficit due to an upstream wind farm may be considerable. If so, energy production loss and mechanical load increase are expected to be significant. For this reason the dedicated planetary boundary layer method Mesoscale Flow with Wind Farming (MFwWF) has been developed, which method computes the interaction between a wind farm and the prevailing wind.

Flow model

The planetary boundary layer method MFwWF is a CFD method that is based on three principles. First, neutral planetary boundary layer flow with wind farming essentially is steady and two-dimensional; where the convective forces, the Coriolis forces, the vertical and spanwise gradients of the turbulent momentum fluxes, and the external forces that represent wind turbines all have the same order of magnitude. Second, a numerical representation of the momentum equations in the form of backward differences allows for an implicit solution of the two horizontal velocity components in vertical direction, iterating on the turbulent viscosity, and a marching solution in the horizontal directions. And third the continuity equation is satisfied by employing the Lagrange multiplier method to the velocity components that satisfy the continuity equation.

Because of its mixed implicit/explicit character the planetary boundary layer method MFwWF is computationally fast and cheap, which is beneficial for applications in wind farm siting studies. In that context MFwWF can be used to estimate the effect of nearby wind farms on the electricity production of a given wind farm.

Effect of a wind farm on the prevailing wind

The planetary boundary layer method MFwWF calculates how a wind farm affects the prevailing wind, or to be more exact, the velocity in a position downstream of a wind farm. To this end wind farm parameters as well as meteorological parameters are considered.

The wind farm parameters include separation distance from and layout of the nearby wind farm, as well as hub height and rotor diameter of the wind turbines in that wind farm. The meteorological parameters include geostrophic velocity, geostrophic height and surface roughness length.

Two of the impact factors are the initial velocity deficit and the velocity recovery distances. The initial velocity deficit is a measure of the energy that is removed from the wind and for that reason a measure of the strength of the wake of the wind farm. The velocity recovery distances - one in downstream direction and the other in spanwise direction relative to the upstream wind direction - measure the distance where the velocity again reaches the upstream value.

As an example the impact of nominal power density and geostrophic velocity on the initial velocity deficit and the downstream velocity recovery distance was studied for a wind farm which consists of 22 wind turbines with a nominal power of 5 MW.

The initial velocity deficit relative to the upstream velocity is found to decrease with increasing geostrophic velocity in general, ranging from 6% (at a turbine separation of 14 rotor diameters) to 100% (at a separation of 5 rotor diameters) if the velocity at hub height is halfway cut-in and nominal.

Also the relative velocity recovery distance is found to decrease with the geostrophic velocity, from a value of 20 at low geostrophic velocities to a limit value near 0 at high geostrophic velocities, and the relative minimum save distance is found to reach a maximum value of the order

of the streamwise wind farm length scale (which maximum is reached at geostrophic velocities between 15 m/s and 25 m/s).

Finally the relative initial velocity deficit is found to decrease with increasing geostrophic velocity, and the largest absolute initial velocity deficit (of in this case 6.3 m/s) is found to occur when the hub-height velocity is near nominal.

Available code

The code MFwWF calculates the effect of one wind farm on another wind farm by taking the entire planetary boundary layer into account. The method has been validated by using measured data from large offshore wind farms, and is available for application to other wind farms.

1. Introduction

Over the years offshore wind farms tend to be placed closer together, as already illustrated by OWEZ and Q7-WF (separated 15 km) in the Netherlands or Horns Rev I and II (separated 23 km) in Denmark. Since these separation distances are between 5 and 10 times the wind farm's horizontal scale, the velocity deficit due to an upstream wind farm may be considerable (Christiansen and Hasager, 2005). If so, energy production loss and mechanical load increase are expected to be significant. For this reason wind farm wake studies have gained attention recently.

In this report we present a new method for determining the interaction between a wind farm and the prevailing wind, and first insights on the modification of the wind field. The new method calculates average values of the wind speed while taking into account the effect of turbulence, and for this reason the first insights on the wind field modification include wind speed deficits only. Actual energy production loss or mechanical load increase however are not presented in this report. First, section 2 gives a brief description of prior work on modeling wind farm wakes. Next section 3 presents a comprehensive description of the new flow model and the corresponding code MWwWF (Mesoscale Flow with Wind Farming), and section 4 addresses the validation. In addition in section 5 predictions obtained with the flow model are addressed. Finally, in section 6 the work is summarized.

2. Prior work

A wind farm wake study requires simulation of mesoscale atmospheric flow together with energy extraction/redistribution due to wind turbines. In this chapter first we present an overview of studies that were published by the year 2007. Next we identify the various approaches in these studies and we finish with a critical review of these approaches.

Liu et al., 1983, developed a numerical model based on the primitive equations in order to study the behaviour of turbulent wakes behind large-scale wind turbines. This model is based on a numerical solution of the Navier-Stokes equations for the planetary boundary layer with the hydrostatic approximation, in combination with a Monin-Obukov description of the turbulent diffusivities. To demonstrate the utility of the model, it was applied to three different configurations of wind turbine arrays, among which one wind turbine immediately downwind of another. The results of the model simulations were found not only to retrieve major features of turbulent wakes observed behind wind turbines but also to compare favorably with corresponding measurements from wind tunnel experiments.

In order to analytically model the effect of a wind farm on the atmospheric boundary layer, Hegberg and Eecen, 2002, first estimate the artificial roughness length of the wind farm. Next they calculate the internal boundary layer which results from the roughness change due to the wind farm. With this information the new turbulent drag force and subsequently the new equilibrium between the forces (turbulent drag force, the Coriolis force and the pressure gradient force) are determined. From that equilibrium the new wind speed and direction are calculated, which are found to be quite different from the conditions outside the wind farm.

Frandsen et al., 2004, developed an analytical model for the flow in and near a wind farm. The model distinguishes between two flow directions (parallel to the rows in a rectangular wind turbine configuration, and not parallel) and identifies three flow regimes (multiple wakes, merging wakes from neighbouring rows, and equilibrium between the wind farm and the boundary layer). The multiple wakes model and the merging wakes model were derived from the Lanchester-Betz theory, whereas the equilibrium model was derived from the geostrophic drag law. The effect of turbulence is included in the modeling of the equilibrium regime only by using the skin friction velocity and the surface roughness length. The model is reported to predict offshore wind recovery distances in the range between 2 and 14 km.

Hegberg et al., 2004, developed a numerical model in order to study the effect of a wind farm on the planetary boundary layer. Similar to their preceding model (Hegberg and Eecen, 2002), a wind farm is modeled as surface roughness but now a number of sub-models is proposed to do so. In addition they add an innovative element in the form of an atmospheric boundary layer model which apart from velocity also takes temperature into account. Turbulence is modeled in terms of Reynolds stresses of velocity and temperature so that the door is opened to treating small departures from the neutral situation.

Baidya Roy et al., 2004, applied the Regional Atmospheric Modeling System model to explore the possible impacts of a large ($100 \times 100 \text{ km}^2$) onshore wind farm in the Great Plains. This model solves the full three-dimensional compressible nonhydrostatic dynamic equations, a thermodynamic equation and a set of microphysics equations. The system of equations is closed with a Mellor-Yamada scheme that explicitly solves for turbulent kinetic energy while other second-order moments are parameterized. A wind turbine was approximated as a sink of energy (operating at a fixed power coefficient of 0.4) and source of turbulence (adding a fixed amount of turbulent kinetic energy), and the wind farm was created by assuming an array of such turbines.

Results show that the wind farm significantly slows down the wind at the turbine hub-height level.

Rooijmans, 2004, simulated the meteorological effects of a large-scale (150x60 km²) offshore wind farm in the North Sea by using the MM5 mesoscale model. The wind farm was simulated by introducing a higher roughness length (0.5 m) in the area of the wind farm. The meteorological effects were examined by comparing model runs with and without wind farm. Turbulent kinetic energy, cloud formation, precipitation and wind speed reduction were studied. As to wind reduction the MM5 model was found to yield comparable results (in and near the wind farm wind speed reduction up to 50% in a high wind speed case) as obtained from a conceptual model which calculates the reduction of horizontal wind speed from a balance between loss of horizontal momentum and replenishment from above by turbulent fluxes.

These studies can be subdivided into two categories: self-similar approaches and mesoscale approaches. In a self-similar approach the convective force and the spanwise turbulent flux gradients are assumed to dominate the flow, allowing for standard wake-like solutions (Frandsen et al., 2004; Hegberg, 2004). In a mesoscale approach, on the other hand, the flow is assumed to be dominated by the Coriolis force and the vertical turbulent flux gradients, opening the door to either extra surface drag approaches (Hegberg, 2002) or more generic mesoscale approaches (Liu et al., 1983; Baidya Roy, 2004; Rooijmans, 2004).

In section 3.3.1 of this report we will show that neither the self-similar wake approach nor the extra surface drag approach is valid because over the separation distance between wind farms the convective and the Coriolis forces are of equal order of magnitude. This implies that a wind farm wake may be deflected. Although this was already implicitly recognized in the more generic approaches, these studies lack realistic formulations for the turbulence and the wind turbines.

3. Flow model

3.1 Overview of the flow modeling approach

We start in section 3.2 with the definition of the flow problem, and subsequently derive the governing equations in section 3.3 and a numerical representation in section 3.4. Next, in section 3.5 we address the continuity equation. We then turn our attention to the turbulence parameterization in section 3.6, and to the wind turbine parameterization in section 3.7. The boundary conditions and initial conditions are presented in section 3.8, and an estimate of the discretisation error in section 3.9. Finally, in section 3.10 we address the translation between grid-cell averaged velocities and point velocities.

3.2 Definition of the flow problem

Consider the geostrophic wind, that is the theoretical wind that results from the balance between the pressure gradient force and the Coriolis force (figure 3.1a). This wind is directed parallel to lines of equal pressure, with low pressure on the left on the northern hemisphere. Turbulent drag slows down the wind and turns it to point towards low pressure. Near the surface the deviation from the geostrophic velocity and direction is largest. Next consider an observer who looks in the direction of the near-surface wind, and introduce the x-axis likewise (figure 3.1b). For this observer the wind points towards the high pressure, which means that in his coordinate system the surface wind has a negative spanwise component. This situation defines the flow problem: To determine the velocity components at a given height as observed when looking in the direction of the near surface wind, given a geostrophic wind and a surface roughness. If the passive observer is replaced by a wind turbine that exerts a force on the wind, the definition of the flow problem is complete (figure 3.1c).

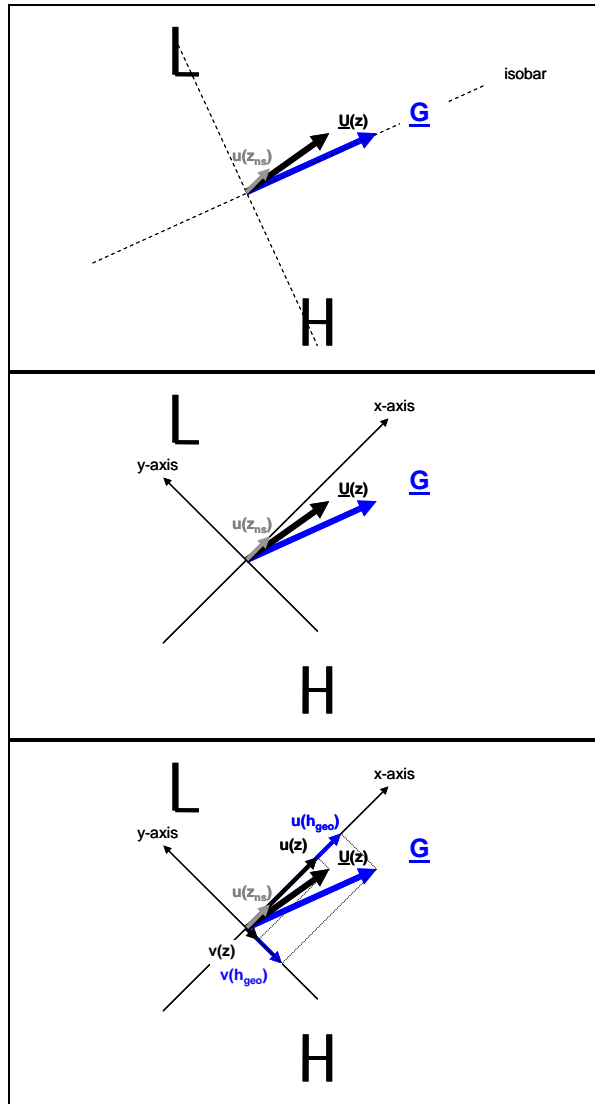


Figure 3.1 *Velocity decomposition. (a) Geostrophic wind G , wind $u(z)$ at a height z above the surface and near-surface wind $u(z_{ns})$. (b) Streamwise axis x in the direction of the near-surface wind. (c) Streamwise component $u(z)$ and spanwise component $v(z)$ of the geostrophic wind*

3.3 Governing equations

3.3.1 Dimensional form

The mean (in the sense of Reynolds averaged) flow in the neutral planetary boundary layer is incompressible and high-Reynolds number. In addition, as explained in section 3.2, it is turbulent and affected by the rotation of the Earth. It is described by the momentum equations (Holton, 1992, section 5.1.2):

$$\frac{\partial \bar{u}}{\partial t} + \bar{u} \frac{\partial \bar{u}}{\partial x} + \bar{v} \frac{\partial \bar{u}}{\partial y} + \bar{w} \frac{\partial \bar{u}}{\partial z} = -\frac{1}{\rho} \frac{\partial \bar{p}}{\partial x} + f_{\phi} \bar{v} - \frac{\partial \overline{u'u'}}{\partial x} - \frac{\partial \overline{u'v'}}{\partial y} - \frac{\partial \overline{u'w'}}{\partial z} + \bar{a}_x \quad (1)$$

$$\frac{\partial \bar{v}}{\partial t} + \bar{u} \frac{\partial \bar{v}}{\partial x} + \bar{v} \frac{\partial \bar{v}}{\partial y} + \bar{w} \frac{\partial \bar{v}}{\partial z} = -\frac{1}{\rho} \frac{\partial \bar{p}}{\partial y} - f_{\phi} \bar{u} - \frac{\partial \overline{v'u'}}{\partial x} - \frac{\partial \overline{v'v'}}{\partial y} - \frac{\partial \overline{v'w'}}{\partial z} + \bar{a}_y \quad (2)$$

$$\frac{\partial \bar{w}}{\partial t} + \bar{u} \frac{\partial \bar{w}}{\partial x} + \bar{v} \frac{\partial \bar{w}}{\partial y} + \bar{w} \frac{\partial \bar{w}}{\partial z} = -\frac{1}{\rho} \frac{\partial \bar{p}}{\partial z} - \frac{\partial \overline{w'u'}}{\partial x} - \frac{\partial \overline{w'v'}}{\partial y} - \frac{\partial \overline{w'w'}}{\partial z} + \bar{a}_z \quad (3)$$

in combination with the continuity equation:

$$\frac{\partial \bar{u}}{\partial x} + \frac{\partial \bar{v}}{\partial y} + \frac{\partial \bar{w}}{\partial z} = 0; \quad (4)$$

and a set of boundary conditions. Here

- \bar{u} , \bar{v} and \bar{w} are the components of the mean velocity;
- u' , v' and w' are the velocity fluctuations;
- ρ is the air density;
- \bar{p} is the mean pressure;
- f_{ϕ} is the Coriolis parameter;
- \bar{a}_x , \bar{a}_y and \bar{a}_z are the mean components of the flow acceleration due to the external body force in this case exerted by wind turbines; and
- the covariances represent the turbulent momentum fluxes.

The z-axis is in vertical direction and without loss of generality the x-axis is assumed to be in the direction of the surface wind. The equations 1, 2, 3 and 4 constitute a system of 4 equations with 4 unknowns, which can be solved once boundary conditions are set. We come back to the boundary conditions in section 3.8.

In order to estimate the magnitude of the individual terms in the equations 1, 2, 3 and 4 we introduce length and velocity scales (Holton, 1992, section 2.4) that correspond to wind farming in the planetary boundary layer (table 3.1). A length scale is a distance related to motions or objects in the planetary boundary layer and a velocity scale is the velocity variation over a given length scale.

Table 3.1 *Scales in the planetary boundary layer with wind farming*

Scale		Value	Magnitude
z_0	Surface roughness length		1 mm - 1 cm
D	Rotor diameter		100 m
S_t	Turbine separation	10 D	1 km
S_f	Wind farm size	10 S_t	10 km
L_x	Wind farm separation	10 S_f	100 km
L_y	Wind farm wake width	10 S_f	100 km
L_z	Planetary boundary layer height		1 km
U_x	x-Velocity variation		10 m/s
U_y	y-Velocity variation		10 m/s
U_z	Vertical velocity variation	0.1 $U_x L_z/L_x$	1 cm/s
Δp	Pressure variation		1 hPa
ΔT	Temporal variation		1 day
u	Velocity variation		1 m/s
ρ	Air density		1 kg/m ³
f_0	Coriolis parameter		10 ⁻⁴ 1/s

First we address the length scales (figure 3.2). The vertical length scales include those of the surface layer (proportional to the surface roughness length), the turbine layer (proportional to the turbine hub height and therefore to the rotor diameter) and the top layer (proportional to the planetary boundary layer height). Since we consider the interaction with wind farms in the planetary boundary layer, the vertical length scale L_z of our flow problem is proportional to the height of the planetary boundary layer. The horizontal length scales include the length of the turbine near wake (proportional to the rotor diameter), the turbine far wake and the related turbine separation (up to 10D), the horizontal scale of a wind farm (typically consisting of 10 rows/columns), and the wind farm wake (up to 10 horizontal wind farm scales). Since we consider motions in the planetary boundary layer due to wind farm wakes, our flow problem has two horizontal length scales: the x-wise length scale L_x which we define to be proportional to the streamwise separation between wind farms, and the y-wise length scale L_y proportional to the width of the wake of a wind farm. Now the vertical length scale L_z is smaller than the horizontal length scales L_x and L_y , and the y-wise length scale L_y is of the same order of magnitude as (but smaller than) the x-wise length scale L_x . Table 3.1 gives the typical values.

As to the velocity scales (figure 3.3), in our flow problem the y-wise velocity scale U_y is of the same order of (but smaller than) the x-wise velocity scale U_x . Since flow on planetary boundary layer scale is approximately horizontal (U_z is smaller than U_x and U_y), inflow in the xy-plane is mainly balanced by outflow in the xy-plane. In other words: the horizontal velocity scales U_x and U_y are of opposite sign. A scale analysis of the continuity equation (table 3.2) gives an upper bound for U_z :

$$U_z \ll \frac{L_z}{L_x} U_x.$$

In the following U_z is an order of magnitude smaller than this upper bound. Another velocity scale is the turbulence velocity scale u , which is of the order of 10% of a horizontal velocity scale. The typical values of the velocity scales are presented in table 3.1. The subsequent scale analysis of the momentum equations 1, 2 and 3 is presented in table 3.3.

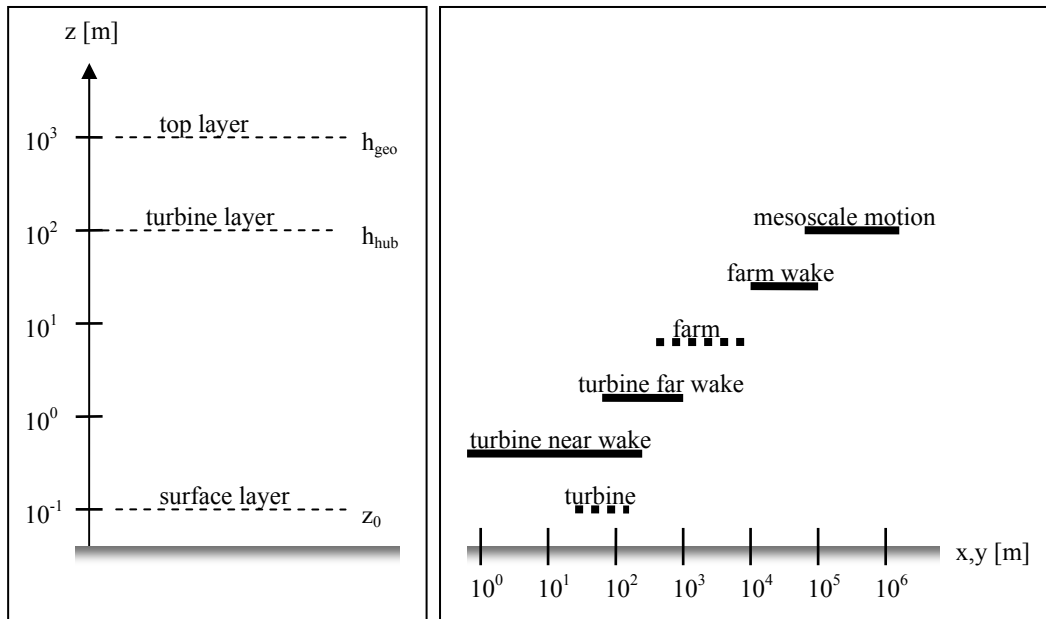


Figure 3.2 Vertical (left) and horizontal (right) length scales

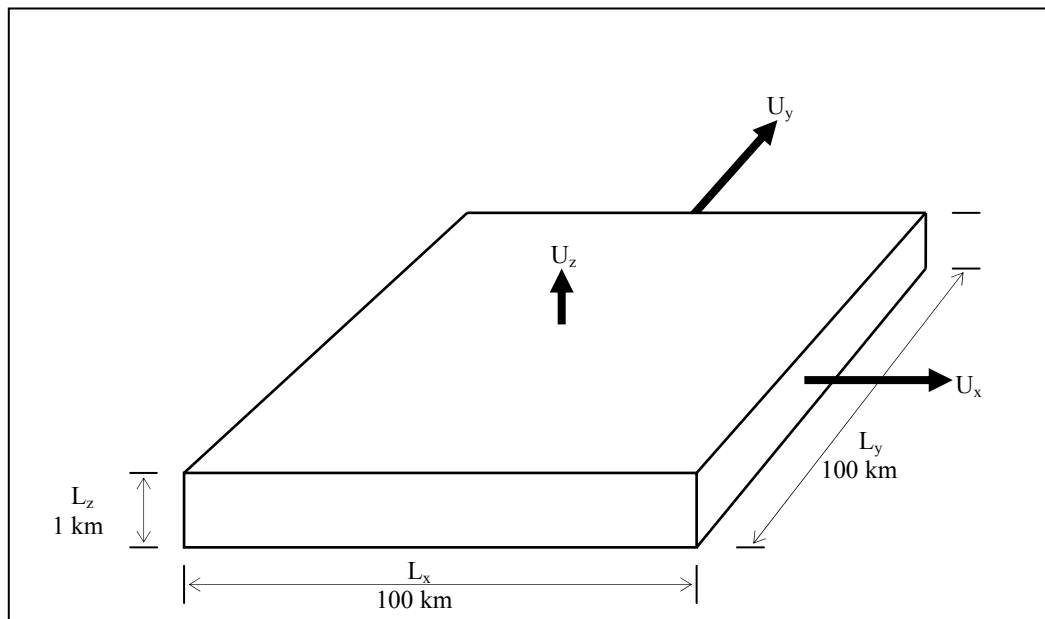


Figure 3.3 Length and velocity scales in the planetary boundary layer with wind farming

Table 3.2 *Scale analysis of the continuity equation*

Continuity	$\frac{\partial \bar{u}}{\partial x}$	$\frac{\partial \bar{v}}{\partial y}$	$\frac{\partial \bar{w}}{\partial z}$
Scale	$\frac{U_x}{L_x}$	$\frac{U_y}{L_y}$	$\frac{U_z}{L_z}$
Magnitude [1/s]	10^{-4}	10^{-4}	$\ll 10^{-4}$

Table 3.3 *Scale analysis of the momentum equation*

x-Momentum	$\frac{\partial \bar{u}}{\partial t}$	$\bar{u} \frac{\partial \bar{u}}{\partial x}$	$\bar{v} \frac{\partial \bar{u}}{\partial y}$	$\bar{w} \frac{\partial \bar{u}}{\partial z}$	$\frac{1}{\rho} \frac{\partial \bar{p}}{\partial x}$	$f_\phi \bar{v}$	$\frac{\partial \overline{u'u'}}{\partial x}$	$\frac{\partial \overline{u'v'}}{\partial y}$	$\frac{\partial \overline{u'w'}}{\partial z}$
Scale	$\frac{U_x}{\Delta T}$	$\frac{U_x^2}{L_x}$	$\frac{U_x U_y}{L_y}$	$\frac{U_x U_z}{L_z}$	$\frac{\Delta p}{\rho L_x}$	$f_\phi U_y$	$\frac{u^2}{L_x}$	$\frac{u^2}{L_y}$	$\frac{u^2}{L_z}$
Magnitude [m/s²]	10^{-4}	10^{-3}	10^{-3}	10^{-4}	10^{-3}	10^{-3}	10^{-5}	10^{-5}	10^{-3}
y-Momentum	$\frac{\partial \bar{v}}{\partial t}$	$\bar{u} \frac{\partial \bar{v}}{\partial x}$	$\bar{v} \frac{\partial \bar{v}}{\partial y}$	$\bar{w} \frac{\partial \bar{v}}{\partial z}$	$\frac{1}{\rho} \frac{\partial \bar{p}}{\partial y}$	$f_\phi \bar{u}$	$\frac{\partial \overline{v'u'}}{\partial x}$	$\frac{\partial \overline{v'v'}}{\partial y}$	$\frac{\partial \overline{v'w'}}{\partial z}$
Scale	$\frac{U_y}{\Delta T}$	$\frac{U_x U_y}{L_x}$	$\frac{U_y^2}{L_y}$	$\frac{U_y U_z}{L_z}$	$\frac{\Delta p}{\rho L_y}$	$f_\phi U_x$	$\frac{u^2}{L_x}$	$\frac{u^2}{L_y}$	$\frac{u^2}{L_z}$
Magnitude [m/s²]	10^{-4}	10^{-3}	10^{-3}	10^{-4}	10^{-3}	10^{-3}	10^{-5}	10^{-5}	10^{-3}
z-Momentum	$\frac{\partial \bar{w}}{\partial t}$	$\bar{u} \frac{\partial \bar{w}}{\partial x}$	$\bar{v} \frac{\partial \bar{w}}{\partial y}$	$\bar{w} \frac{\partial \bar{w}}{\partial z}$	$\frac{1}{\rho} \frac{\partial \bar{p}}{\partial z}$	g	$\frac{\partial \overline{w'u'}}{\partial x}$	$\frac{\partial \overline{w'v'}}{\partial y}$	$\frac{\partial \overline{w'w'}}{\partial z}$
Scale	$\frac{U_z}{\Delta T}$	$\frac{U_x U_z}{L_x}$	$\frac{U_y U_z}{L_y}$	$\frac{U_z^2}{L_z}$	g	$\frac{u^2}{L_x}$	$\frac{u^2}{L_y}$	$\frac{u^2}{L_z}$	
Magnitude [m/s²]	10^{-7}	10^{-6}	10^{-6}	10^{-7}	10	10^{-5}	10^{-5}	10^{-3}	

By neglecting all but one of the small terms (see below) and by employing the definitions

$$f_\phi u_g \equiv -\frac{1}{\rho} \frac{\partial \bar{p}}{\partial y} \quad \text{and} \quad f_\phi v_g \equiv \frac{1}{\rho} \frac{\partial \bar{p}}{\partial x}$$

of the components u_g and v_g of the geostrophic velocity, it follows that also in the case of wind farming the neutral planetary boundary layer equations are essentially steady and two-dimensional:

$$\bar{u} \frac{\partial \bar{u}}{\partial x} + \bar{v} \frac{\partial \bar{u}}{\partial y} = +f_\phi (\bar{v} - v_g) - \frac{\partial \overline{u'v'}}{\partial y} - \frac{\partial \overline{u'w'}}{\partial z} + \bar{a}_x \quad (5)$$

$$\bar{u} \frac{\partial \bar{v}}{\partial x} + \bar{v} \frac{\partial \bar{v}}{\partial y} = -f_\phi (\bar{u} - u_g) - \frac{\partial \overline{v'v'}}{\partial y} - \frac{\partial \overline{v'w'}}{\partial z} + \bar{a}_y \quad (6)$$

convective force	Coriolis force	spanwise turb. flux gradient	vertical turb. flux gradient	external force
---------------------	-------------------	------------------------------------	------------------------------------	-------------------

$$\frac{\partial \bar{u}}{\partial x} + \frac{\partial \bar{v}}{\partial y} = 0 \quad (7)$$

Note that, anticipating on turbulence due to a wind farm, the spanwise gradients $\partial \overline{u'v'}/\partial y$ and $\partial \overline{v'v'}/\partial y$ have been retained although these are an order of magnitude smaller than the other terms in a boundary layer which does not contain a wind farm.

In contrast to standard geostrophic flow, modeled by the momentum equations

$$0 = +f_\phi (\bar{v} - v_g) - \frac{\partial \overline{u'w'}}{\partial z} + \bar{a}_x$$

$$0 = -f_\phi (\bar{u} - u_g) - \frac{\partial \overline{v'w'}}{\partial z} + \bar{a}_y,$$

in the equations 5 and 6 the convective force and the y-wise turbulent momentum flux gradients are significant, which rules out the extra surface drag approaches which are usually applied to solve these momentum equations. In addition, in contrast to general wake flow, modeled by the momentum equations

$$\bar{u} \frac{\partial \bar{u}}{\partial x} + \bar{v} \frac{\partial \bar{u}}{\partial y} = -\frac{\partial \overline{u'v'}}{\partial y} + \bar{a}_x$$

$$\bar{u} \frac{\partial \bar{v}}{\partial x} + \bar{v} \frac{\partial \bar{v}}{\partial y} = -\frac{\partial \overline{v'v'}}{\partial y} + \bar{a}_y,$$

in the equations 5 and 6 the Coriolis force and the vertical turbulent momentum flux gradients are significant, ruling out self-similar wake approaches.

In contrast to the original system the equations 5, 6 and 7 constitute an overdetermined system: 3 equations with 2 unknowns. Since evidently the velocity must obey conservation of mass, the solution to the momentum equations must be corrected in such a way that the velocity satisfies continuity while remaining close to that solution. This is achieved by using the Lagrange mul-

multiplier method (Ferziger and Perić, 1997, section 7.7), which essentially provides the third unknown.

Another scale analysis, the Rossby-number similarity approach (Garra, 1994, section 3.2.1), shows that close to the surface the x-wise velocity component of geostrophic flow is much larger than the y-wise velocity component. At first approximation the near-surface wind is therefore in the x-direction. For this reason in the following the x-direction is referred to as the stream-wise direction, and the y-direction as the spanwise direction. Note this outcome corroborates the definition of the length scales L_x and L_y above.

In order to close the momentum equations 5 and 6 we represent the turbulent momentum fluxes by a mean turbulent viscosity $\overline{k_m}$ in combination with gradients of the mean velocity components:

$$\overline{u'v'} = -\overline{k_m} \left(\frac{\partial \overline{u}}{\partial y} + \frac{\partial \overline{v}}{\partial x} \right), \quad \overline{u'w'} \approx -\overline{k_m} \frac{\partial \overline{u}}{\partial z}, \quad \overline{v'v'} \approx -2\overline{k_m} \frac{\partial \overline{u}}{\partial y} \quad \text{and} \quad \overline{v'w'} \approx -\overline{k_m} \frac{\partial \overline{v}}{\partial z}. \quad (8)$$

The approximations here originate from a scale analysis of the turbulent fluxes (table 3.4) employing the length and velocity scales introduced above (table 3.1). Note the equations are not closed completely because the mean turbulent viscosity remains; its parameterization is addressed in section 3.6.

The external accelerations in the momentum equations 5 and 6 require another form of closure because these accelerations, due to the force exerted by the wind turbines, ultimately depend on the horizontal velocity. We treat this in section 3.7.

By inserting the equations 8 for the turbulent momentum fluxes into the momentum equations 5 and 6, and by applying the continuity equation 7, we obtain:

$$-\overline{u} \frac{\partial \overline{v}}{\partial y} + \overline{v} \frac{\partial \overline{u}}{\partial y} = f_\phi (\overline{v} - v_g) + \frac{\partial \overline{k_m}}{\partial y} \left(\frac{\partial \overline{u}}{\partial y} + \frac{\partial \overline{v}}{\partial x} \right) + \overline{k_m} \left(\frac{\partial^2 \overline{u}}{\partial y^2} + \frac{\partial^2 \overline{v}}{\partial y \partial x} + \frac{\partial^2 \overline{u}}{\partial z^2} \right) + \frac{\partial \overline{k_m}}{\partial z} \frac{\partial \overline{u}}{\partial z} + \overline{a_x} \quad (9)$$

$$\overline{u} \frac{\partial \overline{v}}{\partial x} - \overline{v} \frac{\partial \overline{u}}{\partial x} = -f_\phi (\overline{u} - u_g) + 2 \frac{\partial \overline{k_m}}{\partial y} \frac{\partial \overline{u}}{\partial y} + \overline{k_m} \left(2 \frac{\partial^2 \overline{u}}{\partial y^2} + \frac{\partial^2 \overline{v}}{\partial z^2} \right) + \frac{\partial \overline{k_m}}{\partial z} \frac{\partial \overline{v}}{\partial z} + \overline{a_y} \quad (10)$$

and

$$\frac{\partial \overline{u}}{\partial x} + \frac{\partial \overline{v}}{\partial y} = 0. \quad (11)$$

The momentum equations 9 and 10, together with the continuity equation 11 as the constraint, are the governing equations for neutral planetary boundary layer flow with wind farming.

Table 3.4 *Scale analysis of the turbulent fluxes*

<i>Turbulent fluxes</i>	$\overline{u'v'}$	$\overline{u'w'}$	$\overline{v'v'}$	$\overline{v'w'}$
	$\frac{\partial \bar{u}}{\partial y}$	$\frac{\partial \bar{v}}{\partial x}$	$\frac{\partial \bar{u}}{\partial z}$	$\frac{\partial \bar{w}}{\partial x}$
	$\frac{\partial \bar{v}}{\partial y}$	$\frac{\partial \bar{v}}{\partial z}$	$\frac{\partial \bar{w}}{\partial y}$	$\frac{\partial \bar{w}}{\partial z}$
Scale	$\frac{U_x}{L_y}$	$\frac{U_y}{L_x}$	$\frac{U_x}{L_z}$	$\frac{U_z}{L_x}$
	$\frac{U_y}{L_y}$	$\frac{U_z}{L_z}$	$\frac{U_y}{L_x}$	$\frac{U_z}{L_y}$
Magnitude [1/s]	10^{-4}	10^{-4}	10^{-2}	10^{-7}
	10^{-4}	10^{-2}	10^{-7}	10^{-4}
	10^{-2}	10^{-7}	10^{-4}	10^{-2}
	10^{-7}	10^{-4}	10^{-7}	10^{-7}

3.3.2 Non-dimensional form

Next we introduce the horizontal length scale D (proportional to the wind turbine rotor diameter), the vertical length scale z_0 (proportional to the surface roughness length), and the velocity scale G (proportional to the geostrophic wind velocity), and define:

- The components U and V of the non-dimensional mean velocity:
 $\bar{u} = G U$ and $\bar{v} = G V$ with $G^2 = u_g^2 + v_g^2$;
- The non-dimensional coordinates X , Y and S :
 $x = D X$, $y = D Y$ and $z = z_0 \exp(S)$,
anticipating on a rectangular horizontal grid and a logarithmic vertical grid;
- The non-dimensional mean turbulent viscosity K_m :
 $\bar{k}_m = D G K_m$,
- The components A_x and A_y of the non-dimensional mean external acceleration:
 $\bar{a}_x = \frac{G^2}{D} A_x$ and $\bar{a}_y = \frac{G^2}{D} A_y$.

By inserting these definitions into the equations 9, 10 and 11 we obtain the non-dimensional form of the governing equations:

$$\begin{aligned}
 & -U \frac{\partial V}{\partial Y} + \left(V - \frac{\partial K_m}{\partial Y} \right) \frac{\partial U}{\partial Y} \\
 & = f_p (V - V_g) + \frac{\partial K_m}{\partial Y} \frac{\partial V}{\partial X} + K_m \frac{\partial^2 U}{\partial Y^2} + K_m \frac{\partial^2 V}{\partial Y \partial X} + D_p^2 K_m \frac{\partial^2 U}{\partial S^2} + D_p^2 \left(-K_m + \frac{\partial K_m}{\partial S} \right) \frac{\partial U}{\partial S} + A_x
 \end{aligned} \tag{12}$$

$$\begin{aligned}
 & U \frac{\partial V}{\partial X} - V \frac{\partial U}{\partial X} \\
 & = -f_p (U - U_g) + 2 \frac{\partial K_m}{\partial Y} \frac{\partial U}{\partial Y} + 2 K_m \frac{\partial^2 U}{\partial Y^2} + D_p^2 K_m \frac{\partial^2 V}{\partial S^2} + D_p^2 \left(-K_m + \frac{\partial K_m}{\partial S} \right) \frac{\partial V}{\partial S} + A_y
 \end{aligned} \tag{13}$$

and

$$\frac{\partial U}{\partial X} + \frac{\partial V}{\partial Y} = 0 \quad (14)$$

where $f_p = \frac{f_\phi D}{G}$ and $D_p = \frac{D \exp(-S)}{z_0}$ are non-dimensional parameters.

3.4 Momentum equations

3.4.1 Discretization

Anticipating on an explicit solution of the momentum equation in a given point we discretize the equations 12 and 13 in the grid point $[i,j,k]$ with backward finite differences employing grid sizes ΔX , ΔY and ΔS_k . (Recall the vertical coordinates are non-equidistant.) Doing so, the non-linear terms cancel:

$$\begin{aligned} & -U \frac{\partial V}{\partial Y} + \left(V - \frac{\partial K_m}{\partial Y} \right) \frac{\partial U}{\partial Y} \\ & \approx U[i,j,k] \frac{V[i,j-1,k]}{\Delta Y} - V[i,j,k] \frac{U[i,j-1,k]}{\Delta Y} - \frac{\partial K_m}{\partial Y} \frac{U[i,j,k] - U[i,j-1,k]}{\Delta Y} \\ & = \frac{1}{\Delta Y} \left(V[i,j-1,k] - \frac{\partial K_m}{\partial Y} \right) U[i,j,k] - \frac{U[i,j-1,k]}{\Delta Y} V[i,j,k] + \frac{\partial K_m}{\partial Y} \frac{U[i,j-1,k]}{\Delta Y} \end{aligned}$$

and

$$\begin{aligned} & U \frac{\partial V}{\partial X} - V \frac{\partial U}{\partial X} \\ & \approx -\frac{V[i-1,j,k]}{\Delta X} U[i,j,k] + \frac{U[i-1,j,k]}{\Delta X} V[i,j,k], \end{aligned}$$

where the approximations originate from neglecting the truncation errors. Omitting the identifier $[i,j]$ for ease of notation, in a given point $[i,j,k]$ the resulting difference equations have the following form:

$$A_u[k] U[k] + B_u[k] V[k] = C_u[k] U[k-1] + D_u[k] U[k-2] + E_u[k]$$

$$A_v[k] U[k] + B_v[k] V[k] = C_v[k] V[k-1] + D_v[k] V[k-2] + E_v[k];$$

which is equivalent to:

$$\begin{pmatrix} D_u[k] & 0 \\ 0 & D_v[k] \end{pmatrix} \begin{pmatrix} U[k-2] \\ V[k-2] \end{pmatrix} + \begin{pmatrix} C_u[k] & 0 \\ 0 & C_v[k] \end{pmatrix} \begin{pmatrix} U[k-1] \\ V[k-1] \end{pmatrix} + \begin{pmatrix} -A_u[k] & -B_u[k] \\ -A_v[k] & -B_v[k] \end{pmatrix} \begin{pmatrix} U[k] \\ V[k] \end{pmatrix} = \begin{pmatrix} -E_u[k] \\ -E_v[k] \end{pmatrix}. \quad (15)$$

The system of equations 15 is the already announced explicit solution of the momentum equation in a given point. The coefficients A, B, C, D and E "only" depend on:

- The grid sizes ΔX , ΔY and ΔS_k of the numerical domain,
- The turbulent viscosity in the point $[i,j,k]$ and its spanwise and vertical gradients,
- The components of the flow acceleration due to the external force, and
- The velocity components in the backward points $[i,j-1,k]$, $[i-1,j,k]$, $[i-1,j-1,k]$, $[i,j-2,k]$.

Together this implies that if the turbulent viscosity is computed separately (see section 3.6), the external acceleration is known (see section 3.7) and the indicated backward velocities are available, the system of equations 15 allows for an implicit solution of U and V in a vertical at $[i,j]$ once appropriate boundary conditions are set.

At the bottom of the numerical domain ($k = 1: z = z_0$) the boundary condition is no slip, so that, on omitting the identifier $[i,j]$ for ease of notation, we get:

$$\begin{pmatrix} C_u[3] & 0 \\ 0 & C_v[3] \end{pmatrix} \begin{pmatrix} U[2] \\ V[2] \end{pmatrix} + \begin{pmatrix} -A_u[3] & -B_u[3] \\ -A_v[3] & -B_v[3] \end{pmatrix} \begin{pmatrix} U[3] \\ V[3] \end{pmatrix} = \begin{pmatrix} -E_u[3] \\ -E_v[3] \end{pmatrix}.$$

At the top ($k = k_{\max}: z = h_{\text{geo}}$ that is the height where the velocity reaches the geostrophic value) the velocity is geostrophic, so that:

$$\begin{aligned} & \begin{pmatrix} D_u[k_{\max}] & 0 \\ 0 & D_v[k_{\max}] \end{pmatrix} \begin{pmatrix} U[k_{\max}-2] \\ V[k_{\max}-2] \end{pmatrix} + \begin{pmatrix} C_u[k_{\max}] & 0 \\ 0 & C_v[k_{\max}] \end{pmatrix} \begin{pmatrix} U[k_{\max}-1] \\ V[k_{\max}-1] \end{pmatrix} \\ & = \begin{pmatrix} -E_u[k_{\max}] \\ -E_v[k_{\max}] \end{pmatrix} + \begin{pmatrix} A_u[k_{\max}] & B_u[k_{\max}] \\ A_v[k_{\max}] & B_v[k_{\max}] \end{pmatrix} \begin{pmatrix} U_g \\ V_g \end{pmatrix}, \end{aligned}$$

where $U_g = u_g / G$ and $V_g = v_g / G$ are the non-dimensional components of the geostrophic velocity.

3.4.2 Representation

By employing for ease of notation the matrix-vector equivalent of the system of equations 15:

$$\underline{D}[k] \underline{U}[k-2] + \underline{C}[k] \underline{U}[k-1] + \underline{AB}[k] \underline{U}[k] = \underline{E}[k],$$

the momentum system in the vertical at $[i,j]$ is:

$$\underline{M} \underline{U}_m = \underline{c}; \tag{16}$$

with the matrix of size $2(k_{\max}-2) \times 2(k_{\max}-2)$:

$$\underline{\underline{M}} = \begin{pmatrix} \underline{\underline{C}}[3] & \underline{\underline{AB}}[3] & 0 & 0 & \dots & 0 & 0 & 0 \\ \underline{\underline{D}}[4] & \underline{\underline{C}}[4] & \underline{\underline{AB}}[4] & 0 & \dots & 0 & 0 & 0 \\ 0 & \underline{\underline{D}}[5] & \underline{\underline{C}}[5] & \underline{\underline{AB}}[5] & \dots & 0 & 0 & 0 \\ \dots & \dots \\ 0 & 0 & 0 & 0 & \dots & \underline{\underline{D}}[k_{\max}-1] & \underline{\underline{C}}[k_{\max}-1] & \underline{\underline{AB}}[k_{\max}-1] \\ 0 & 0 & 0 & 0 & \dots & 0 & \underline{\underline{D}}[k_{\max}] & \underline{\underline{C}}[k_{\max}] \end{pmatrix}$$

and the vectors

$$\underline{U}_m = \begin{pmatrix} \underline{U}_m[2] \\ \underline{U}_m[3] \\ \underline{U}_m[4] \\ \dots \\ \underline{U}_m[k_{\max}-2] \\ \underline{U}_m[k_{\max}-1] \end{pmatrix} \quad \text{and} \quad \underline{c} = \begin{pmatrix} \underline{E}[3] \\ \underline{E}[4] \\ \underline{E}[5] \\ \dots \\ \underline{E}[k_{\max}-1] \\ \underline{E}[k_{\max}] - \underline{\underline{AB}}[k_{\max}] \underline{U}_g \end{pmatrix}.$$

The index m denotes that the velocities satisfy the momentum equation.

3.4.3 Solution procedure

Since the velocity depends on the turbulent viscosity, the solution procedure iterates between solving the relatively small matrix-vector system in equation 16 by Gaussian elimination and computing the turbulent viscosity profile. The procedure starts in the vertical at $[i+1, j+2]$ so that initial velocity conditions are needed at the inlet plane $i = 1$ and the two planes at $j = 1$ and $j = 2$, and initial turbulent viscosity conditions at $[i, j]$. Once a vertical profile of U and V is computed in $[i, j]$, the procedure proceeds with the profiles in $[i, j+1]$, $[i, j+2]$ etc. until j_{\max} is reached. Next the planes at $i+1$, $i+2$ etc up to i_{\max} follow. The solution therefore marches in the two horizontal directions.

3.4.4 Formal order of the numerical scheme

In order to estimate the formal order of the numerical scheme we cast the momentum system in equation 15 into the matrix-vector form and consider the truncation error in its solutions U and V while isolating the various error sources.

The matrix-vector representation of the momentum system is:

$$\underline{\underline{AB}} \underline{U} = \underline{R} \quad (17)$$

with

$$\underline{\underline{AB}} = \begin{pmatrix} A_u + A_u^1 \Delta y & B_u + B_u^1 \Delta y \\ A_v + A_v^1 \Delta x & B_v + B_v^1 \Delta x \end{pmatrix}, \quad \underline{U} = \begin{pmatrix} U \\ V \end{pmatrix}, \quad \text{and} \quad \underline{R} = \begin{pmatrix} R_u + R_u^1 \Delta z^2 \\ R_v + R_v^1 \Delta z^2 \end{pmatrix};$$

where

$$\begin{aligned} A_u \text{ etc indicate the elements of the momentum matrix,} \\ A'_u \text{ etc indicate the coefficients in the leading term of truncation errors, and} \\ R_u = D_u[k]U[k-2] + C_u[k]U[k-1] + E_u[k] \text{ and} \\ R_v = D_v[k]V[k-2] + C_v[k]V[k-1] + E_v[k] \text{ are the elements of the vector } \underline{R}. \end{aligned}$$

Now we consider the streamwise velocity U . By applying Cramer's rule to the system in equation 17, it follows that:

$$U = \frac{D_u + \Delta D_u}{D + \Delta D}$$

with

$$\begin{aligned} D_u &= R_u B_v - R_v B_u \\ \Delta D_u &= R_u B'_v \Delta x - R_v B'_u \Delta y + (B_v R'_u - B_u R'_v) \Delta z^2 + (B'_v R'_u \Delta x - B'_u R'_v \Delta y) \Delta z^2, \end{aligned}$$

and

$$\begin{aligned} D &= A_u B_v - A_v B_u \\ \Delta D &= (A_u B'_v - b_u A'_v) \Delta x + (b_v A'_u - A_v B'_u) \Delta y + (A'_u B'_v - A'_v B'_u) \Delta x \Delta y. \end{aligned}$$

Recognizing the exact solution D_u/D , we subsequently introduce the discretization error ΔU in the streamwise velocity:

$$\Delta U \equiv \frac{D_u + \Delta D_u}{D + \Delta D} - \frac{D_u}{D} \approx \frac{D \Delta D_u - D_u \Delta D}{D^2} \left(1 + \frac{\Delta D}{D} \right). \quad (18)$$

In order to isolate the contribution by the truncation error in the vertical direction we set $\Delta X = 0$ and $\Delta Y = 0$. As a result we obtain:

$$\Delta D_u = (B_v R'_u - B_u R'_v) \Delta z^2 \quad \text{and} \quad \Delta D = 0.$$

By inserting these values into equation 18 it follows that the discretization error ΔU is proportional to the square of the vertical grid size:

$$\Delta U = \frac{\Delta D_u}{D} = \frac{B_v R'_u - B_u R'_v}{A_u B_v - A_v B_u} \Delta z^2.$$

Next we consider two discretization errors: ΔU_2 on the vertical grid ΔZ_2 and ΔU_1 on ΔZ_1 . Their ratio is given by:

$$\frac{\Delta U_2}{\Delta U_1} = \frac{\Delta Z_2^2}{\Delta Z_1^2}. \quad (19)$$

By introducing the definition of the order p_z of the vertical scheme and by inserting equation 19 in this definition it can be shown that the formal order of the numerical scheme in vertical direction is:

$$p_z \equiv \frac{\ln \frac{\Delta U_2}{\Delta U_1}}{\ln \frac{\Delta Z_2}{\Delta Z_1}} = 2.$$

In order to isolate the contribution to ΔU by the truncation error in spanwise direction we set $\Delta X = 0$ and $\Delta Z = 0$, with as a result:

$$\Delta D_u = -R_v B_u^1 \Delta y \quad \text{and} \quad \Delta D = (B_v A_u^1 - A_v B_u^1) \Delta y.$$

By inserting these values into equation 18 it follows that:

$$\Delta U = \frac{D \Delta D_u - D_u \Delta D}{D^2} \left(1 + \frac{\Delta D}{D} \right) = \alpha \Delta y + \beta \Delta y^2$$

with

$$\alpha = -(A_u B_v - A_v B_u) R_v B_u^1 - (R_u B_v - R_v B_u) (B_v A_u^1 - A_v B_u^1)$$

$$\beta = R_v B_u^1 (B_v A_u^1 - A_v B_u^1);$$

where the two terms in ΔU are found to be of the same order of magnitude. The ratio between the discretization errors ΔU_2 and ΔU_1 on the spanwise grid sizes ΔY_2 and ΔY_1 is:

$$\frac{\Delta U_2}{\Delta U_1} = \frac{\alpha \Delta y_2 + \beta \Delta y_2^2}{\alpha \Delta y_1 + \beta \Delta y_1^2}. \quad (20)$$

By using equation 20 it can be shown that the formal order p_y of the scheme in spanwise direction is:

$$p_y \equiv \frac{\ln \frac{\Delta U_2}{\Delta U_1}}{\ln \frac{\Delta Y_2}{\Delta Y_1}} = \frac{\ln \frac{\alpha \Delta y_2 + \beta \Delta y_2^2}{\alpha \Delta y_1 + \beta \Delta y_1^2}}{\ln \frac{\Delta Y_2}{\Delta Y_1}} \approx \frac{\ln \frac{\Delta Y_2}{\Delta Y_1} + \frac{\beta}{\alpha} (\Delta Y_2 - \Delta Y_1)}{\ln \frac{\Delta Y_2}{\Delta Y_1}} \quad \text{with} \quad \frac{\alpha}{\beta} = \left(\frac{A_u}{A_v} - \frac{R_u}{R_v} \right) \frac{B_v}{B_u^1}.$$

By evaluating the value of the matrix elements and the vector elements in equation 17 it can be shown that

$$\frac{\beta}{\alpha} \propto \frac{\partial^2 u}{\partial y^2} \frac{\Delta z^4}{\Delta x} \frac{v}{k_m^2},$$

where $\partial^2 u / \partial y^2$ indicates the curvature of the streamwise velocity, v indicates the spanwise velocity and k_m indicates the turbulent viscosity.

Subsequently the range of possible values of p_y is estimated by evaluating two limit situations: 1) near the bottom and 2) near the top of the numerical domain. Near the bottom of the numerical domain β/α is found to vanish because of the low values of the spanwise velocity in combination with the small vertical grid size, with as a consequence that p_y approaches 1 in that region. Near the top of the numerical domain $\beta/(\alpha \partial^2 u / \partial y^2)$ is found to approach -1 so that p_y approaches -0.5 there.

In order to isolate the contribution to ΔU by the truncation error in streamwise direction we set $\Delta Y = 0$ and $\Delta Z = 0$. Proceeding in a similar way as for p_y it can be shown that the possible values of the order p_x of the numerical scheme in streamwise direction are $-0.5 < p_x < 1$ too.

Finally we consider the spanwise velocity V . By proceeding in the same way as for U similar expressions are obtained for the order of the schemes in the vertical, the spanwise and the streamwise direction.

3.4.5 Numerical stability

To investigate the numerical stability of the momentum system in equation 15, we consider the matrix-vector representation of equation 17 while neglecting the truncation errors.

In general an error in a matrix element will propagate into an error in the resolved vector. For example if the matrix element A_u is disturbed by an error e , the propagation of this error is given by the growth vector:

$$\begin{pmatrix} g_u \\ g_v \end{pmatrix} \equiv \frac{\underline{\underline{\varepsilon}}}{e} = \frac{1}{|\underline{\underline{AB}}|^2} \left[1 + \frac{B_v}{|\underline{\underline{AB}}|} e \right]^{-1} \begin{pmatrix} -B_v^2 & B_v B_u \\ B_v A_v & A_v B_u \end{pmatrix} \begin{pmatrix} R_u \\ R_v \end{pmatrix} \quad \text{with} \quad \underline{\underline{\varepsilon}} = \begin{pmatrix} U^* - U \\ V^* - V \end{pmatrix},$$

where $\underline{\underline{\varepsilon}}$ is the vector with the errors in the resolved vector. Similar expressions can be derived for a disturbance of the other matrix elements.

In order to prevent instability we require that the absolute value of the growth rate remains smaller than 1:

$$-1 < g_u < +1 \quad \text{and} \quad -1 < g_v < +1 .$$

At the bottom of the numerical domain, where errors grow from initial velocities $\bar{u} \approx 0$ and $\bar{v} \approx 0$, it can be shown this requirement is met if

$$\frac{\min(\Delta x, \Delta y)}{\Delta z_{\min}^4} \geq c_{b1} \frac{f_\phi \max(|u_g|, |v_g|)}{\bar{k}_m^2(z_0)}, \quad (21)$$

where Δz_{\min} indicates the spacing between the lower two points in vertical direction, c_{b1} indicates a constant of proportionality and $\bar{k}_m(z_0)$ indicates the mean turbulent viscosity at the bottom of the numerical domain. Equation 21 reveals that for the solution procedure to remain stable the horizontal grid sizes must be *larger* than a critical value which is proportional to the vertical grid size and the value of the Coriolis parameter, and which is inversely proportional to the turbulent viscosity. With the exponential vertical grid expansion $z = z_0 \exp(S)$ and the assumption

$$\bar{k}_m(z_0) \propto -\frac{z_0 u_g}{\ln(z_0 / h_{\text{geo}})}$$

from equation 21 it follows that:

$$\frac{\min(\Delta X, \Delta Y)}{(\exp(\Delta S) - 1)^4} \geq c_b \frac{z_0^2 f_\phi}{G D} \ln^2 \frac{z_0}{h_{\text{geo}}} \max(|U_g|, |V_g|).$$

At the top of the numerical domain, on the other hand, errors grow from initial velocities $\bar{u} \approx u_g$ and $\bar{v} \approx v_g$ and the requirement on preventing error propagation is met if

$$\frac{\min(2\Delta x - \Delta y, 2\Delta y - \Delta x)}{\Delta z_{\text{max}}^2} \geq c_{t1} \frac{\max(|u_g|, |v_g|)}{\bar{k}_m(h_{\text{geo}})}, \quad (22)$$

where Δz_{max} indicates the spacing between the upper two points in vertical direction, c_{t1} indicates a constant of proportionality and $\bar{k}_m(h_{\text{geo}})$ is the mean turbulent viscosity at the top of the numerical domain. With the exponential vertical grid expansion and the assumption that $\bar{k}_m(h_{\text{geo}}) \propto c_{\text{Nik}} h_{\text{geo}} G$, from equation 22 it follows that:

$$\frac{\min(2\Delta X - \Delta Y, 2\Delta Y - \Delta X)}{(1 - \exp(-\Delta S))^2} \geq \frac{c_t}{c_{\text{Nik}}} \frac{h_{\text{geo}}}{D} \max(|U_g|, |V_g|).$$

As an illustration figure 3.4 shows the empirically determined minimal horizontal grid size for different combination of the geostrophic height and the surface roughness length in the case of a geostrophic wind speed of 14.1 m/s.

3.4.6. Conservation of mass and energy

The solution to the matrix-vector momentum system in equation 16 does not automatically satisfy the continuity and the energy equations. In this section we derive an optimal solution in the sense that it is mass and energy conserving, and at the same time remains close to the momentum conserving solution.

Conservation of mass requires (recall equation 14):

$$\frac{\partial U}{\partial X} + \frac{\partial V}{\partial Y} = 0,$$

which in the grid point $[i, j, k]$ reduces to:

$$\frac{U[i, j, k] - U[i-1, j, k]}{\Delta X} + \frac{V[i, j, k] - V[i, j-1, k]}{\Delta Y} = 0. \quad (23)$$

Equation 23 implies that given the preceding values $U[i-1, j, k]$ and $V[i, j-1, k]$, in $[i, j, k]$ a mass conserving solution must satisfy:

$$A U[i, j, k] + B V[i, j, k] + C = 0 \quad (24)$$

with

$$A = \frac{1}{\Delta X}, \quad B = \frac{1}{\Delta Y}, \quad \text{and} \quad C = -\frac{U[i-1, j, k]}{\Delta X} - \frac{V[i, j-1, k]}{\Delta Y},$$

which is a line in the UV-plane.

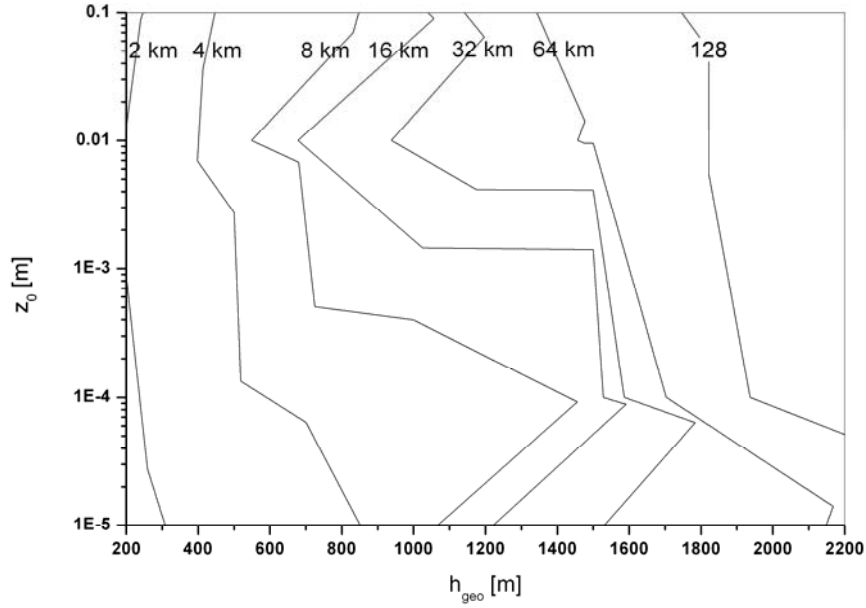


Figure 3.4 *Minimal horizontal grid spacing for different combination of the geostrophic height and the surface roughness length*

Conservation of energy requires

$$\frac{\partial e}{\partial x} \Delta x + \frac{\partial e}{\partial y} \Delta y + \frac{\partial e}{\partial z} \Delta z + e_{\text{ext}} = 0 \quad \text{with} \quad e \approx \frac{1}{2} \rho (U^2 + V^2).$$

It can be shown that in the grid point $[i,j,k]$ an energy conserving solution must satisfy:

$$a U^2[i,j,k] + b V^2[i,j,k] + c U[i,j,k] V[i,j,k] + d U[i,j,k] + e V[i,j,k] + f = 0 \quad (25)$$

with

$$a = b = 2, \quad c = \frac{\Delta x}{\Delta y} + \frac{\Delta y}{\Delta x}, \quad d = V[i,j-1,k] \frac{\Delta x}{\Delta y} - U[i,j-1,k] - U[i,j,k-1],$$

$$e = U[i-1,j,k] \frac{\Delta y}{\Delta x} - V[i-1,j,k] - V[i,j,k-1] \quad \text{and} \quad f = -\frac{1}{2} \rho E[i,j,k];$$

which is a closed contour in the UV-plane.

In general there are two solutions $(U_{\text{ma\&en}}, V_{\text{ma\&en}})$ which satisfy equation 24 and equation 25 simultaneously. The optimal solution is the vector (U, V) which is halfway between the solution $(U_{\text{mo}}, V_{\text{mo}})$ of the momentum equation and the nearest value of $(U_{\text{ma\&en}}, V_{\text{ma\&en}})$. This is illustrated in figure 3.5.

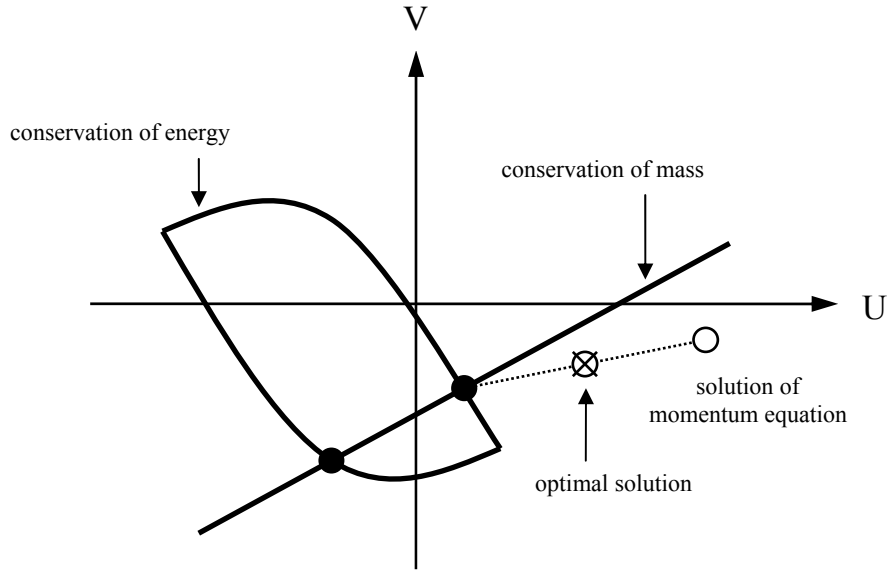


Figure 3.5 *Optimal solution of the flow problem*

3.5 Continuity equation revisited

3.5.1 Lagrange multiplier method

The optimal solution does not automatically satisfy the continuity equation. In order to derive a velocity that does satisfy continuity we apply the Lagrange multiplier method (Ferziger and Perić, section 7.7). This method basically provides the third unknown to the system of equations by applying a Poisson solver to the divergence of the velocity field, and subsequently computes the gradient of the so-determined third unknown.

Now consider the components \bar{u}_m and \bar{v}_m of the velocity that satisfy the momentum equations. According to the Lagrange multiplier method the third unknown λ is given by

$$\frac{\partial^2 \lambda}{\partial x^2} + \frac{\partial^2 \lambda}{\partial y^2} + \frac{\partial^2 \lambda}{\partial z^2} = \frac{\partial \bar{u}_m}{\partial x} + \frac{\partial \bar{v}_m}{\partial y}, \quad (26)$$

with Neuman boundary conditions

$$\frac{\partial \lambda}{\partial x} = 0 \quad \text{and} \quad \frac{\partial \lambda}{\partial y} = 0$$

at the faces of the computational domain because a correction to the velocity is not needed there. The gradient of the third unknown is equal to the velocity correction, so that

$$\bar{u}_{c+m} = \bar{u}_m - \frac{\partial \lambda}{\partial x} \quad \text{and} \quad \bar{v}_{c+m} = \bar{v}_m - \frac{\partial \lambda}{\partial y}$$

are the components of the velocity that satisfy both momentum and continuity.

$$\underline{\underline{G}}_k = \begin{pmatrix} \begin{matrix} d_k & a & & & & & \\ a & d_k & a & & & & \\ & & \ddots & \ddots & \ddots & & \\ & & & a & d_k & a & \\ & & & & & a & d_k \\ & & & & & & \\ & & & & & & \end{matrix} & \begin{matrix} b & & & & & & \\ & b & & & & & \\ & & \ddots & \ddots & \ddots & & \\ & & & b & & & \\ & & & & b & & \\ & & & & & b & \\ & & & & & & \end{matrix} & & & \\ \begin{matrix} b & & & & & & \\ & b & & & & & \\ & & \ddots & \ddots & \ddots & & \\ & & & b & & & \\ & & & & b & & \\ & & & & & b & \\ & & & & & & \end{matrix} & \begin{matrix} d_k & a & & & & & \\ a & d_k & a & & & & \\ & & \ddots & \ddots & \ddots & & \\ & & & a & d_k & a & \\ & & & & & a & d_k \\ & & & & & & \\ & & & & & & \end{matrix} & \begin{matrix} b & & & & & & \\ & b & & & & & \\ & & \ddots & \ddots & \ddots & & \\ & & & b & & & \\ & & & & b & & \\ & & & & & b & \\ & & & & & & \end{matrix} & & \\ & & \begin{matrix} b & & & & & & \\ & b & & & & & \\ & & \ddots & \ddots & \ddots & & \\ & & & b & & & \\ & & & & b & & \\ & & & & & b & \\ & & & & & & \end{matrix} & \begin{matrix} d_k & a & & & & & \\ a & d_k & a & & & & \\ & & \ddots & \ddots & \ddots & & \\ & & & a & d_k & a & \\ & & & & & a & d_k \\ & & & & & & \\ & & & & & & \end{matrix} & \begin{matrix} b & & & & & & \\ & b & & & & & \\ & & \ddots & \ddots & \ddots & & \\ & & & b & & & \\ & & & & b & & \\ & & & & & b & \\ & & & & & & \end{matrix} & \\ & & & \begin{matrix} b & & & & & & \\ & b & & & & & \\ & & \ddots & \ddots & \ddots & & \\ & & & b & & & \\ & & & & b & & \\ & & & & & b & \\ & & & & & & \end{matrix} & \begin{matrix} d_k & a & & & & & \\ a & d_k & a & & & & \\ & & \ddots & \ddots & \ddots & & \\ & & & a & d_k & a & \\ & & & & & a & d_k \\ & & & & & & \\ & & & & & & \end{matrix} \end{pmatrix}$$

and

$$\underline{\underline{H}}_k = c_k \underline{\underline{I}}.$$

It is clear that $\underline{\underline{P}}$ is sparse and has 7 bands. Unlike a standard Poisson matrix, the bands -3 and $+3$ as well as the band 0 (the diagonal) have a structure because of the non-equidistant vertical grid. In addition, $\underline{\underline{P}}$ is not diagonally dominant because of the logarithmic vertical grid in combination with the Neumann boundary condition at the bottom of the numerical domain.

3.5.3 Solution procedure

The matrix-vector system in equation 27 is solved iteratively:

$$\underline{\underline{\Lambda}}^{(i)} = \left[\underline{\underline{I}} - (\underline{\underline{D}}_p + \underline{\underline{\Delta}})^{-1} \underline{\underline{P}} \right] \underline{\underline{\Lambda}}^{(i-1)} + (\underline{\underline{D}}_p + \underline{\underline{\Delta}})^{-1} \underline{\underline{R}},$$

which only involves cheap row operations because of the structure of $\underline{\underline{P}}$. In this scheme $\underline{\underline{D}}_p$ is the diagonal matrix of $\underline{\underline{P}}$, and $\underline{\underline{\Delta}}_p$ is the defect matrix which without loss of generality is chosen to be equal to $f \underline{\underline{D}}_p$, where f is a positive factor. The function of the defect matrix is to alleviate the not-diagonally dominant character of $\underline{\underline{P}}$, and by doing so to improve the convergence rate of the iterations. The stopping criterion is:

$$\frac{\| \underline{\underline{P}} \underline{\underline{\Lambda}}^{(i)} - \underline{\underline{R}} \|_2}{\| \underline{\underline{R}} \|_2} \leq \varepsilon,$$

where ε is a threshold.

3.6 Turbulence parameterization

The mean turbulent viscosity in the momentum equations 9 and 10 is parameterized by using a modified version of the algebraic Baldwin-Lomax model, where the modification consists of a new formulation of the mixing length in combination with parameters which are calibrated such that realistic values of the turbulence intensity occur.

The mean turbulent viscosity \overline{k}_m is [Willcox, section 3.4.2]:

$$\overline{k}_m = \min[\overline{k}_{m,i}, \overline{k}_{m,o}],$$

where $\overline{k}_{m,i}$ and $\overline{k}_{m,o}$ are the inner and outer layer turbulent viscosity, respectively.

The inner layer turbulent viscosity depends on the mixing length λ_{mix} and the mean vorticity $\overline{\omega}$:

$$\overline{k}_{m,i} = \lambda_{\text{mix}}^2 \overline{\omega}. \quad (28)$$

The mixing length in equation 28 is given by

$$\lambda_{\text{mix}} = \min \left[z_0 + C_{\text{cal}} \kappa z \left[1 - \exp\left(-\frac{z}{A_0}\right) \right], C_{\text{Nik}} h_{\text{geo}} \right]$$

with

$$C_{\text{cal}} = A_x \left[1 - \exp\left(-\frac{z_{10m}}{A_0}\right) \right]^{-1} \quad \text{and} \quad A_0 = \frac{\nu}{u_*} A_0^+.$$

Here C_{cal} is a calibration parameter, A_x is the Dutton-Panofsky parameter (see below), A_0 is the Van Driest coefficient rescaled to the surface roughness length z_0 ; ν is the kinematic viscosity and u_* is the friction velocity. Note that the modified model uses the surface roughness length as the minimal value of the mixing length and the Van Driest function in order to limit the growth of the mixing length, and limits the mixing length to the fraction C_{Nik} of the geostrophic height in agreement with observations of Nikuradse (Nikuradse, 1932; cited in Schlichting, 1979, section XX.c).

The vorticity in equation 28 is given by

$$\overline{\omega}^2 \approx \left(\frac{\partial \overline{u}}{\partial y} - \frac{\partial \overline{v}}{\partial x} \right)^2 + \left(\frac{\partial \overline{u}}{\partial z} \right)^2 + \left(\frac{\partial \overline{v}}{\partial z} \right)^2.$$

The outer layer turbulent viscosity $\overline{k}_{m,o}$ depends on the wake turbulent viscosity $\overline{k}_{m,w}$ and employs the Klebanoff function so that the turbulent viscosity decreases with distance from the surface in the outer layer:

$$\overline{k}_{m,o} = \alpha C_c \left[1 + C_{\kappa 2} \left(\frac{C_{\kappa 1} z}{h_{\text{mix}}} \right)^6 \right]^{-1} \overline{k}_{m,w}.$$

Table 3.5 *Coefficients in the modified Baldwin-Lomax model*

κ	α	C_c	$C_{\kappa 1}$	$C_{\kappa 2}$	C_w	A_0^+	C_{Nik}
0.41	0.0168	κ/α	0.3	5.5	1.0	26	0.14

Table 3.6 *Dutton-Panofsky parameter according to Dyrbye and Hansen*

z_0	A_x
0.05	2.5
0.3	1.8

The wake turbulent viscosity is the smaller of two viscosities that are defined on basis of a turbulent mixing velocity v_{mix} , the distance h_{mix} above the surface where the turbulent mixing velocity is largest, and the velocity $U_{h_{mix}}$ at h_{mix} :

$$\overline{k_{m,w}} = \min[\overline{k_{m,w1}}, \overline{k_{m,w2}}] \text{ with } \overline{k_{m,w1}} = h_{mix} v_{mix,max} \text{ and } \overline{k_{m,w2}} = C_w h_{mix} \frac{U_{h_{mix}}^2}{v_{mix,max}}$$

where

$$v_{mix,max} = \max_z[v_{mix}] \text{ with } v_{mix} = \frac{\lambda_{mix} \overline{\omega}}{\kappa} \text{ and } U_{h_{mix}}^2 \equiv \overline{u}^2(h_{mix}) + \overline{v}^2(h_{mix}) .$$

Note that at the surface the turbulent viscosity has a small but non-zero value in agreement with the concept of a hydraulic rough wall. At the top of the numerical domain, where the velocity reaches the geostrophic value, turbulent viscosity is non-zero in agreement with observations by Nikuradse.

The standard value 2.4 of the Dutton-Panofsky parameter A_x was found to give too small a value of the turbulence intensity and for that reason also of the turbulent viscosity. For this reason A_x is interpolated/extrapolated to the surface roughness length by using the values reported in the literature (Dyrbye and Hansen, 1997).

The modified Baldwin-Lomax algebraic parameterization is preferred over one or two-equation parameterizations (like the $k\epsilon$ or the $k\omega$ model) because, apart from being simple to implement, it is a turbulent boundary layer parameterization containing the elementary physics (mean vorticity as the primary source of turbulent viscosity so that it varies with vertical as well as streamwise and spanwise velocity gradients).

3.7 Wind turbine parameterization

The external acceleration in the momentum equation is due to the force exerted on the flow by a cluster of wind turbines. Apart from the sign this force is equal to the sum of the thrust on the individual rotors. The rotor thrust of a single wind turbine essentially depends on the velocity induced by the rotor of that wind turbine, which in turn is related to the power production and thus to the horizontal velocity at hub height. Evidently the external acceleration is only present in a grid point where wind turbine are located or the grid points where turbines are interpolated; it is zero in any other grid point.

The external acceleration due to a *single* wind turbine is determined as follows. First, the vertical profile of the velocity components U and V is computed with the external acceleration set to zero, yielding the "undisturbed" horizontal velocity U_{hub} at hub height and the corresponding direction φ_{hub} :

$$U_{\text{hub}}^2 \equiv \bar{u}^2(h_{\text{hub}}) + \bar{v}^2(h_{\text{hub}}) \quad \text{and} \quad \varphi_{\text{hub}} \equiv \arctan\left(\frac{\bar{v}(h_{\text{hub}})}{\bar{u}(h_{\text{hub}})}\right).$$

Then, by using the power curve $P(U)$ of the wind turbine, via the implicit relation between the power coefficient and the induction factor, the induction factor a is computed:

$$a(1-a)^2 = \frac{2}{\pi \rho} \frac{P(U_{\text{hub}})}{U_{\text{hub}}^3 D^2}.$$

The induction factor due to the single wind turbine is subsequently employed to determine the streamwise component A_x and the spanwise component A_y of the flow acceleration due to the wind turbine:

$$A_x = A \frac{\bar{u}(h_{\text{hub}})}{U_{\text{hub}}} \quad \text{and} \quad A_y = A \frac{\bar{v}(h_{\text{hub}})}{U_{\text{hub}}}$$

with

$$A \equiv \frac{D \bar{a}}{G^2} = -\frac{4}{5} \left(\frac{U_{\text{hub}}}{G}\right)^2 a(1-a) = -\frac{1}{5} \left(\frac{U_{\text{hub}}}{G}\right)^2 C_T.$$

Note that alternatively the flow acceleration per unit volume can be computed directly if the thrust curve of the wind turbine is available.

The external acceleration due to a *cluster* of wind turbines subsequently is determined by multiplying the single turbine value with the number of turbines N_t . In the grid point $[i,j,k]$ the flow acceleration is

$$A[i,j,k] = w_H[i,j] w_V[k] N_t A,$$

where w_H is the fraction of $\Delta x \Delta y$ covered by the horizontal area with wind turbines, w_V is the fraction of $\Delta y \Delta z[k]$ covered by the rotor swept area, and Δx , Δy and $\Delta z[k]$ are the sizes of the grid cell.

3.8 Initial and boundary conditions

3.8.1 Boundary conditions

Mean velocity boundary conditions have already been introduced in section 3.3.1: zero at the bottom of the numerical domain (corresponding to z_0) and geostrophic at its top (corresponding to h_{geo}). The boundary conditions for the mean turbulent viscosity are included in its parameterization (see section 3.6): vanishing but non-zero at both the bottom and the top of the numerical domain.

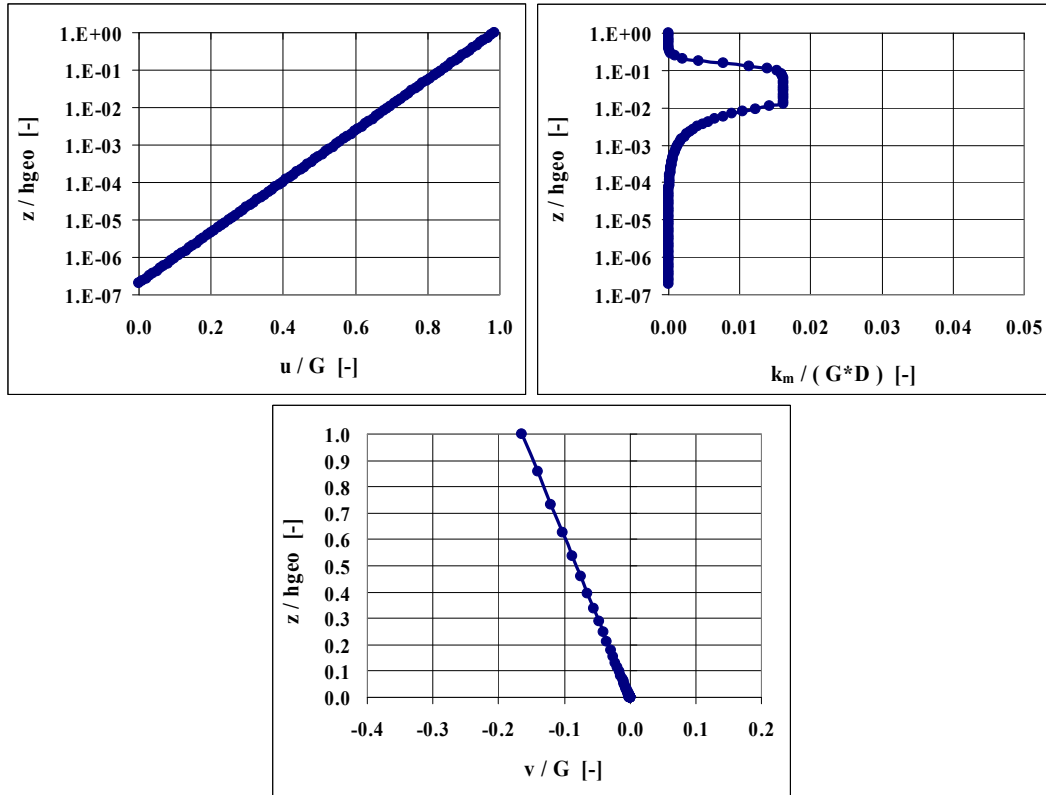


Figure 3.6 *Initial profiles of streamwise velocity u , spanwise velocity v and turbulent viscosity k_m as made non-dimensional with the geostrophic velocity G , the geostrophic height h_{geo} and the rotor diameter D ; geostrophic height of 500 m and surface roughness length 0.1 mm*

3.8.2 Initial conditions

Velocity initial conditions are needed in the inlet plane $i = 1$ and in the planes $j = 1$ and $j = 2$. These are inspired by the Rossby-number similar planetary boundary layer velocity profiles [Garra, 1994, section 3.2.1], and comprise a logarithmic profile for the non-dimensional streamwise velocity

$$U(z) = \left(1 - \frac{\ln(z/h_{geo})}{\ln(z_0/h_{geo})} \right) \frac{u_g}{G} \quad (29)$$

and a linear profile for the non-dimensional spanwise velocity:

$$V(z) = \frac{z - z_0}{h_{geo} - z_0} \frac{v_g}{G}, \quad (30)$$

where z is the distance from the surface.

The initial profile for the mean turbulent viscosity, also needed in the vertical at $[i, j]$, is obtained by applying the Baldwin-Lomax model to the profiles according to the equations 29 and 30.

As an example figure 3.6 shows the initial profiles for a geostrophic height of 500 m and a surface roughness length of 0.1 mm.

3.9 Estimate of discretization error

In this section we give estimates of the discretization error in the numerical solution by using the Richardson method [Ferziger and Perić, 1997, section 3.10]. First the procedure is introduced and next the estimates are given.

The discretization error ε_h is the difference between the exact solution Φ and the numerical solution φ_h , and generally is expressed as the sum of the first and the higher order terms in the Taylor expansion of the exact solution:

$$\varepsilon_h \equiv \Phi - \varphi_h = \alpha h^p + \text{h.o.t.} \quad (31)$$

Here α is a constant (in the sense that it does not depend on the grid spacing), h is the grid spacing and p is the leading order of the discretization error.

The order p and the constant α can be estimated if a numerical solution is available on three grids with different spacing h , mh and nh :

$$\frac{m^p - 1}{n^p - 1} = \frac{\varphi_h - \varphi_{mh}}{\varphi_h - \varphi_{nh}} \quad \text{and} \quad \alpha = \frac{\varphi_h - \varphi_{mh}}{(m^p - 1) h^p}.$$

(Note the often quoted explicit relation $p = \ln((\varphi_h - \varphi_{mh})/(\varphi_h - \varphi_{nh}))/\ln(m/n)$ only is valid if $m^p \gg 1$ and $n^p \gg 1$.) By inserting these estimates into equation 31 it follows that estimates for the discretization error on the finer grid and the corresponding relative discretization error are:

$$\varepsilon_h \approx \alpha h^p = \frac{\varphi_h - \varphi_{mh}}{m^p - 1} \quad \text{and} \quad \frac{\varepsilon_h}{\varphi_h} = \frac{1}{m^p - 1} \left[1 - \frac{\varphi_{mh}}{\varphi_h} \right].$$

Table 3.7 shows the observed order and error for the implicit scheme that is used in the vertical direction. Data from two different finest grids are presented (209 and 417 points), both with the same grid ratios ($m = 2.0035$ and $n = 4.0344$). The calculations were performed with a boundary layer which has a geostrophic velocity of 14.1 m/s, a geostrophic height of 200 m and a surface roughness length of 1 mm; the domain is 200 x 200 km². Recalling the estimated formal order $p_z = 2$ (section 3.4.4), the data in table 3.7 show that the observed order is smaller than the formal order. The data also show that acceptable values of the relative discretization error require a relative large number of grid points in vertical direction.

Table 3.8 shows the observed order and error for the explicit scheme that is used in the horizontal directions, on basis of a finest grid with 57 points in streamwise and spanwise direction and with grid ratios $m = 2$ and $n = 4$. Now recall the range of possible values of the estimated formal order is $-0.5 < p_{x,y} < 1$ (section 3.4.4). Near the top and near the bottom the observed order is found to be in agreement with the formal order in the sense that it has a negative value, but close to the bottom the observed order does not correspond to the formal order. Note that a relative small number of grid points are sufficient to get small values of the relative discretization error.

Table 3.7 *Order p and error ε of the scheme in vertical direction at three vertical positions (near the top, near the bottom and close to the bottom). Subscripts indicate streamwise resp. spanwise velocity*

z/h_{geo}	$N_z = 209$				$N_z = 417$			
	p_u	ε_u	p_v	ε_v	p_u	ε_u	p_v	ε_v
	[-]	[-]	[-]	[-]	[-]	[-]	[-]	[-]
0.625	1.5	0.023	1.7	0.029	1.3	0.012	1.3	0.017
0.153	1.3	0.053	1.5	0.076	1.2	0.027	1.2	0.044
$8 \cdot 10^{-6}$	0.9	0.161	2.8	0.025	1.0	0.060	1.1	0.035

Table 3.8 *Order p and error ε of the scheme in horizontal direction at three vertical positions (near the top, near the bottom and close to the bottom). Subscripts indicate streamwise resp. spanwise velocity*

z/h_{geo}	$N_x = 57, N_y = 57$			
	p_u	ε_u	p_v	ε_v
	[-]	[-]	[-]	[-]
0.625	-1.0	-0.001	-1.0	-0.027
0.153	-1.0	-0.002	-1.0	-0.043
$8 \cdot 10^{-6}$	-2.6	-0.001	-0.5	-0.065

3.10 Translation from grid-cell averaged velocity to point velocity

Because of the discretization a solution to the matrix-vector system provides the grid-cell averaged value of the velocity vector, which value in the wake of the wind farm can not automatically be compared to the point value of the velocity vector. In this section we derive a translation between the grid-cell averaged velocity and the point velocity downstream of a wind farm, and two measures of the impact of a wind farm on the point velocity.

Inspired by the literature (e.g. Barthelmie et al, 2003; Elliot, 1991; Milborrow, 1980), we introduce a point velocity wake model which has a power law decay in streamwise direction d_x and a Gaussian decay in spanwise direction d_y (see figure 3.7 for an explanation):

$$U(d_x, d_y) = U_0 - \Delta U(d_x, d_y) \quad \text{with} \quad \frac{\Delta U(d_x, d_y)}{\Delta U_{\text{ini}}} = \left(\frac{d_x}{d} \right)^m \exp \left\{ - \frac{d_y^2}{(b_1 d_x + b_0)^2} \right\}. \quad (32)$$

Here m is the exponent of the streamwise velocity deficit decay, ΔU_{ini} is the initial velocity deficit, $d = 2D$ is the streamwise scale of the velocity deficit decay, b_1 is the decay rate of the wake width, and b_0 is the initial wake width.

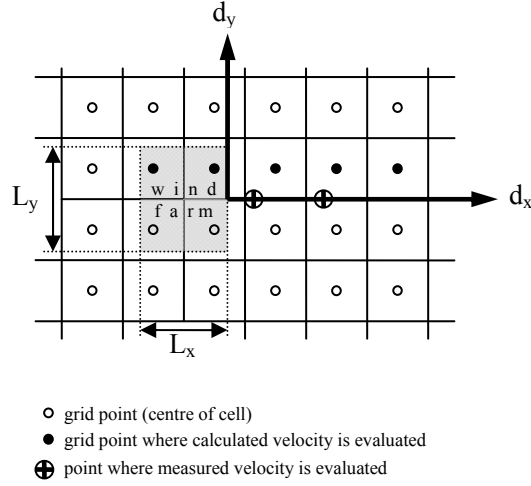


Figure 3.7 Horizontal lay-out of the grid cells in relation to the horizontal area covered by the wind farm, and definition sketch of downstream distance d_x , spanwise distance d_y , streamwise wind farm length scale L_x and spanwise wind farm length scale L_y . Also indicated are the points where measured velocity is evaluated in the validation study

The grid-cell averaged streamwise velocity U_{III} in the first grid cell behind the wind farm is obtained by integrating the point velocities over the horizontal domain:

$$\Delta x \Delta y U_{III} = \int_{d_x=x_1}^{x_2} \int_{d_y=y_1}^{y_2} U(d_x, d_y) dd_x dd_y,$$

where $x_1 = \Delta x - L_x/2$, $x_2 = 2\Delta x - L_x/2$, $y_1 = 0$ and $y_2 = \Delta y$. Here Δx and Δy indicate the horizontal sizes of the grid cell, and L_x indicates the streamwise length of the wind farm. It can be shown that

$$U_{III} = U_0 - \frac{\sqrt{\pi}}{2\Delta x \Delta y} \frac{d}{m+1} f_{III} e_{III} \Delta U_{ini} \quad (33)$$

$$\text{with } f_{III} = s_2 \left(\frac{x_2}{d} \right)^{m+1} - s_1 \left(\frac{x_1}{d} \right)^{m+1} - \frac{b_1 d}{m+1} \left(\left(\frac{x_2}{d} \right)^{m+2} - \left(\frac{x_1}{d} \right)^{m+2} \right) \text{ and } e_{III} = \text{erf}(t_2);$$

where $s_2 = b_1 x_2 + b_0$, $s_1 = b_1 x_1 + b_0$ and $t_2 = y_2 / s_2$.

In a similar way the grid-cell averaged streamwise velocity U_{IV} in the second grid cell behind the wind farm is obtained:

$$U_{IV} = U_0 - \frac{\sqrt{\pi}}{2\Delta x \Delta y} \frac{d}{m+1} f_{IV} e_{IV} \Delta U_{ini} \quad (34)$$

$$\text{with } f_{IV} = s_3 \left(\frac{x_3}{d} \right)^{m+1} - s_2 \left(\frac{x_2}{d} \right)^{m+1} - \frac{b_1 d}{m+1} \left(\left(\frac{x_3}{d} \right)^{m+2} - \left(\frac{x_2}{d} \right)^{m+2} \right) \text{ and } e_{IV} = \text{erf}(t_3);$$

where $x_3 = 3\Delta x - x_F/2$, $s_3 = b_1 x_3 + b_0$ and $t_3 = y_2 / s_3$.

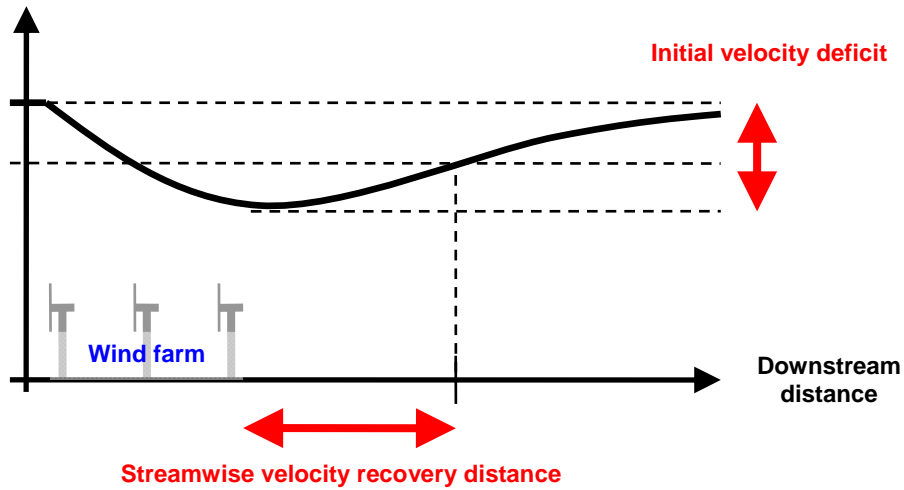


Figure 3.8 *Illustration of the concepts of initial velocity deficit and streamwise velocity recovery distance*

The equations 33 and 34 constitute a system of two equations with the two unknowns m and ΔU_{ini} . The exponent m is resolved from the rewritten system:

$$\frac{U_{III} - U_0}{U_{IV} - U_0} = \frac{f_{III} e_{III}}{f_{IV} e_{IV}},$$

and subsequently the initial velocity deficit ΔU_{ini} is obtained from:

$$\Delta U_{ini} = -\frac{U_{III} - U_{IV}}{f_{III} e_{III} - f_{IV} e_{IV}} \frac{2(m+1) \Delta x \Delta y}{\sqrt{\pi} d}.$$

The exponent m of the streamwise velocity deficit decay and the initial velocity deficit ΔU_{ini} in combination with the point velocity model in equation 32 conveniently allow one to define two measures of the impact of the wind farm on the velocity: the velocity recovery distance (see figure 3.8) and the minimum save distance.

The velocity recovery distance d_{VR} is defined as the distance where the velocity deficit has decayed to 1% of the upstream velocity:

$$\frac{d_{VR}}{2D} = \left(\frac{1}{100} \frac{U_0}{\Delta U_{ini}} \right)^{\frac{1}{m}}.$$

The minimum save distance d_{MS} is defined as the distance where the velocity deficit has decayed to 0.5 m/s:

$$\frac{d_{MS}}{2D} = \left(\frac{\Delta U_{msd}}{\Delta U_{ini}} \right)^{\frac{1}{m}} \text{ with } \Delta U_{msd} = 0.5 \text{ m/s}.$$

4. Validation

In this chapter we address validation of the planetary boundary layer method that is described in chapter 3. Validation data consists of 10-minute averaged point velocities measured at or near hub height at met masts located upstream and downstream of the Horns Rev wind farm and the Nysted wind farm¹. In both cases we compare the resolved point velocities obtained from the calculated grid-cell averaged values by using the method introduced in section 3.10.

The Horns Rev wind farm consists of 80 wind turbines with a hub height of 70 m, a rotor diameter of 80 m and a nominal power of 2 MW. It covers an area of approximately 20 km², and has wind turbine rows directed 90-270 deg (from West to East). The Nysted wind farm, on the other hand, consists of 72 wind turbines with a hub height of 69 m and a rotor diameter of 84 m. These turbines can operate at two modes, reaching the full nominal power of 2.3 MW at one mode but a lower nominal power of 0.4 MW at the other. Nysted covers an area of approximately 23 km², and has rows directed 98-278 deg.

Figure 4.1 shows the velocity W relative to the upstream velocity W_{ups} as a function of the downstream distance d_x from the Horns Rev wind farm for upstream velocities of 6 m/s, 8 m/s and 10 m/s in combination with wind directions near 270 deg. In the calculations the surface roughness length is 0.1 mm, the geostrophic height is 500 m, and the geostrophic velocity is set such that the correct velocity at hub height is obtained. The number of grid points in vertical direction is 100. The calculated velocities are average values in grid cells with a horizontal area of 3.92 x 3.92 km² and the centre at a spanwise distance of 1.96 km at a height of 66 m. Also indicated are the resolved point velocities as obtained by using an initial wake width $b_0 = L_x/3$ (where L_x indicates the spanwise length of the wind farm) and a wake-width decay rate $b_1 = 1/35$. The measured velocities, which are not shown because of confidentiality reasons, on the other hand, are point values at a spanwise distance zero and at downstream distances of 2 km and 6 km at a height of 70 m. Upstream turbulent intensities have the same order of magnitude in the calculations and in the measurements (10% resp. between 7% and 8%).

The figure 4.1 shows that the calculated relative velocity deficit $(W_{\text{ups}}-W)/W_{\text{ups}}$ is smaller than the resolved one and by doing so illustrates the different character of these velocity deficits. These are larger than the calculated velocity deficits and in fact come within 5% of the resolved velocity deficits. Note that both the calculated as the measured relative velocity deficits are found to *increase* with increasing upstream velocity for the cases with 6 m/s and 8 m/s.

Calculations with higher values of the surface roughness length and/or the geostrophic height did not give significantly different results.

¹ Measured data by courtesy of L.E. Jensen of Dong Energy A/S as prepared by K.S. Hansen in the framework of the European UPWIND research project under contract with the European Commission (CE Contract Number 019945 (SES6))

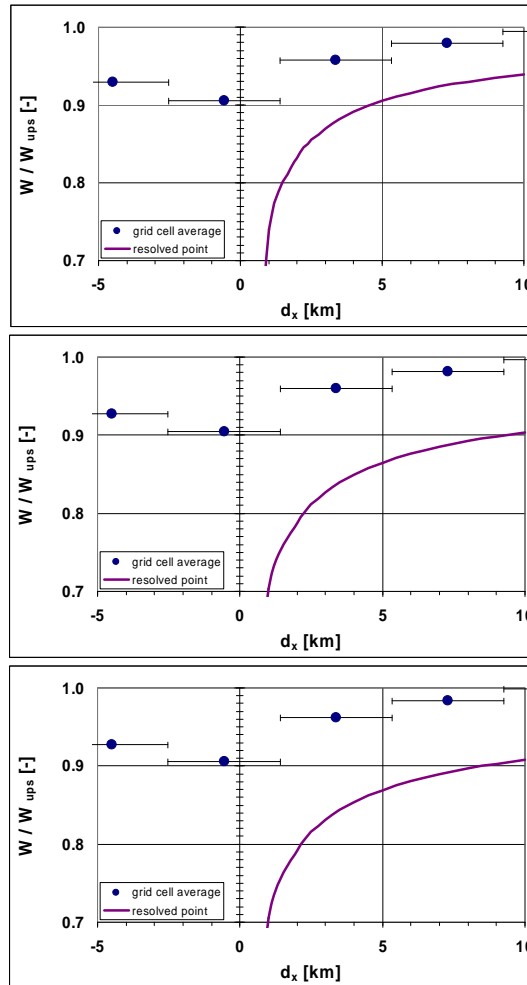


Figure 4.1 *Velocity W relative to the upstream velocity W_{ups} as a function of distance d_x downstream the Horns Rev wind farm. The upstream velocity is 6 m/s (top), 8 m/s (centre) and 10 m/s (bottom). Horizontal error bars indicate the streamwise size of the grid cell. Displayed are the grid-cell averaged velocity and the resolved point velocity*

In order to explore the velocity wake of the Horns Rev wind farm, table 4.1 presents the exponent m of the streamwise velocity deficit decay and the initial velocity deficit ΔU_{ini} relative to the upstream velocity U_0 as derived from the calculations by using the method introduced in section 3.10. These values are found to come close to the measured values (which are not shown): within 6% for the exponent and within 17% for the initial velocity deficit².

² Note that from theoretical considerations "possible" values of the exponent of the wake expansion law can be identified (Tennekes and Lumley, 1972, table 4.1). According to these the actual value of the exponent depends on the type of wake, distinguishing between the wake behind a propelled or a not-propelled body on the one hand and between an axisymmetric or a plane wake on the other hand:

	axi-symm	plane
not-propelled body	-2/3	-1/2
propelled body	-4/5	-3/4

This suggests that, depending on the collective loading of the turbines and the asymmetry of the wake, values in the range between -0.5 and -0.8 are possible. Also note measurements behind a single wind turbine indicate an exponent of -1.04 ± 0.07 (e.g. Barthelmie et al. 2003)

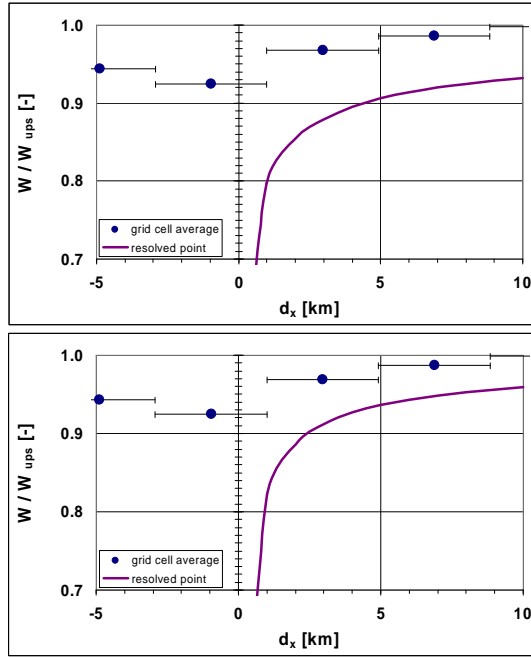


Figure 4.2 Velocity W relative to the upstream velocity W_{ups} as a function of distance d_x downstream the Nysted wind farm. The upstream velocity is 8 m/s (top) and 10 m/s (bottom). Horizontal error bars indicate the streamwise size of the grid cell. Displayed are the grid-cell averaged velocity and the resolved point velocity

Table 4.1 Point values of the exponent m of the streamwise velocity deficit decay and the initial velocity deficit ΔU_{ini} as resolved from the calculated velocities

		m [-]	$\Delta U_{ini}/U_0$ [-]
		resolved	resolved
Horns Rev	6 m/s	-0.629	0.825
	8 m/s	-0.488	0.726
	10 m/s	-0.503	0.740
Nysted	8 m/s	-0.477	0.476
	10 m/s	-0.640	0.557

Table 4.2 Velocity recovery distance d_{VR} and the minimum save distance d_{MS} , as calculated from the data in table 4.1

		d_{VR} [km]	d_{MS} [km]
Horns Rev	6 m/s	178	6.1
	8 m/s	1047	24.4
	10 m/s	832	33.9
Nysted	8 m/s	554	6.5
	10 m/s	90	5.1

Figure 4.2 shows the same information for the Nysted wind farm for upstream velocities of 8 m/s and 10 m/s in combination with wind directions near 278 deg. Apart from the wind turbine and the wind farm data the input to the calculations is the same as for the Horns Rev case. The velocities are measured at downstream distances of 2 km and 5 km at a height of 69 m. Measured upstream turbulent intensity is between 7% and 9%.

The data in figure 4.2 reveal much the same information as in figure 4.1 but with one exception: the relative velocity deficits are found to *decrease* with increasing upstream velocity for the cases with 6 m/s and 8 m/s.

Another look at the impact of the wind farms on the velocity is offered by the velocity recovery distance d_{VR} and the minimum save distance d_{MS} , see table 4.2. It is found that d_{VR} is of the order of 100...1000 kilometers, whereas d_{MS} is of the order of 10 kilometers.

In conclusion, resolved relative velocity deficits (point values which originate from the calculated grid cell averaged velocity deficits) have been found to come close to the relative velocity deficits that have been measured in the wake of the Horns Rev and the Nysted wind farms. The same holds for the corresponding impact measures (velocity recovery distance and minimum save distance).

5. Predictions

5.1 Overview of predictions

In this chapter we address predictions, which are outcome of calculations which can not be compared to measured data. First, in section 5.2 resolved velocity profiles are presented for the empty set, a single wind turbine, and a wind farm. Next, in section 5.3 the impact of wind farm design parameters and meteorological design parameters on the wind is presented.

5.2 Resolved velocity profiles

5.2.1 Empty set

Resolved velocity profiles for the empty set comprise a domain without wind turbines or wind farms. Figure 5.1 shows four vertical profiles, each in a corner of a $200 \times 200 \text{ km}^2$ domain as valid for a geostrophic height of 500 m and a surface roughness length of 0.1 mm. (The corners are conveniently labeled NorthWest, NorthEast, SouthEast and SouthWest, where the mean flow is directed to the East.) The number of grid points in vertical direction is 25. The figures display the streamwise velocity versus height, the spanwise velocity, the angle between the streamwise and the spanwise velocity, and a hodograph of the two velocity components. The data in the figure is in qualitative agreement with the observed height dependence of undisturbed wind, where most of the velocity change occurs in the lower part and most of the direction change occurs in the upper part of the boundary layer, but it is too early to decide on the quantitative agreement.

The figures 5.2 and 5.3 display a much thicker boundary layer (1500 m) with the same surface roughness, and the same boundary layer thickness in combination with a much rougher surface (1 cm). The figures show that the thinner the boundary layer or the larger the surface roughness, the larger the twist in the velocity profile. Again there is a qualitative agreement with observations which is to be collaborated with quantitative data.

5.2.2 Wind turbine

The modification of the wind profile due to a hypothetical wind turbine is studied for a turbine with a nominal power of 5 MW operating at full load, and having a rotor diameter of 100 m and a hub height of 70 m. Figure 5.4 shows that the relative initial velocity deficit is of the order of 5% and that the velocity twist is increased with 1...2 deg. The velocity recovery distance d_{rec} is of the order of 100 rotor diameters.

5.2.3 Wind farm

The hypothetical wind farm consists of 22 turbines with a rotor diameter of 100 m, a hub height of 70 m and a nominal power of 5 MW. The turbine separation distance is 1 km (10 rotor diameters) so that the nominal power density is 5 MW/km^2 . It operates in a boundary layer with a geostrophic height of 500 m and a surface roughness length of 0.1 mm; the hub-height velocity corresponds to about 64% of the geostrophic velocity. Figure 5.5 shows that if the wind farm operates at full load the initial velocity deficit is of the order of 15% and that the velocity twist is increased with 2...3 deg. The velocity recovery distance is at least 2 streamwise wind farm length scales L_x .

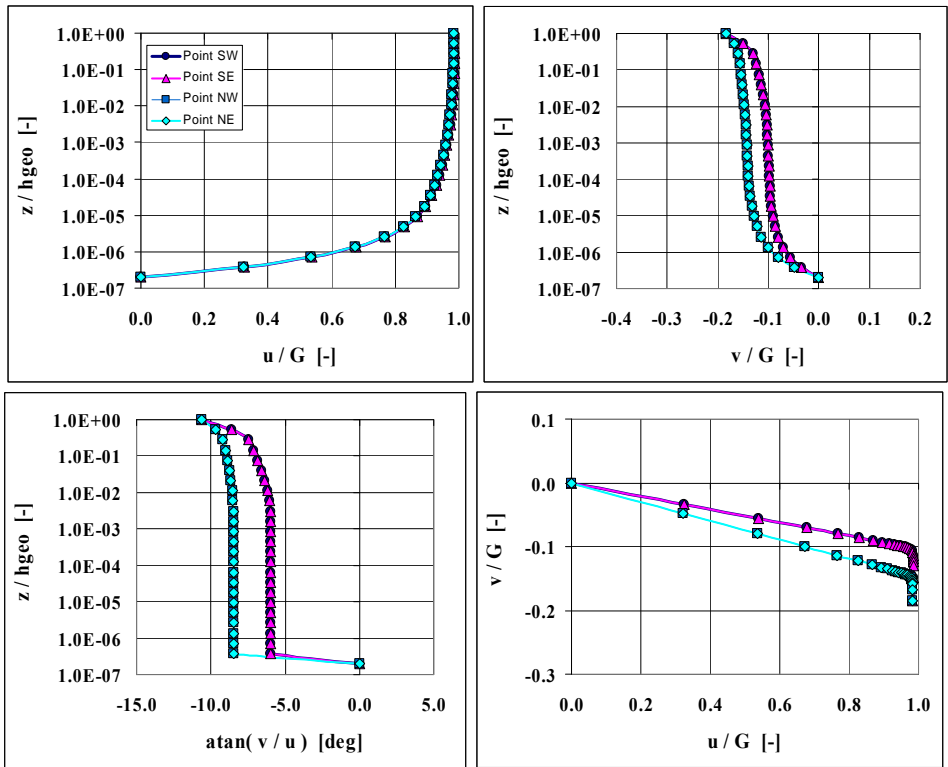


Figure 5.1 *Vertical profiles of streamwise velocity u and spanwise velocity v in the four corners NorthWest, NorthEast, SouthEast and SouthWest of the numerical domain as made non-dimensional with the geostrophic velocity G and the geostrophic height h_{geo} ; valid for a geostrophic height of 500 m and a surface roughness length of 0.1 mm*

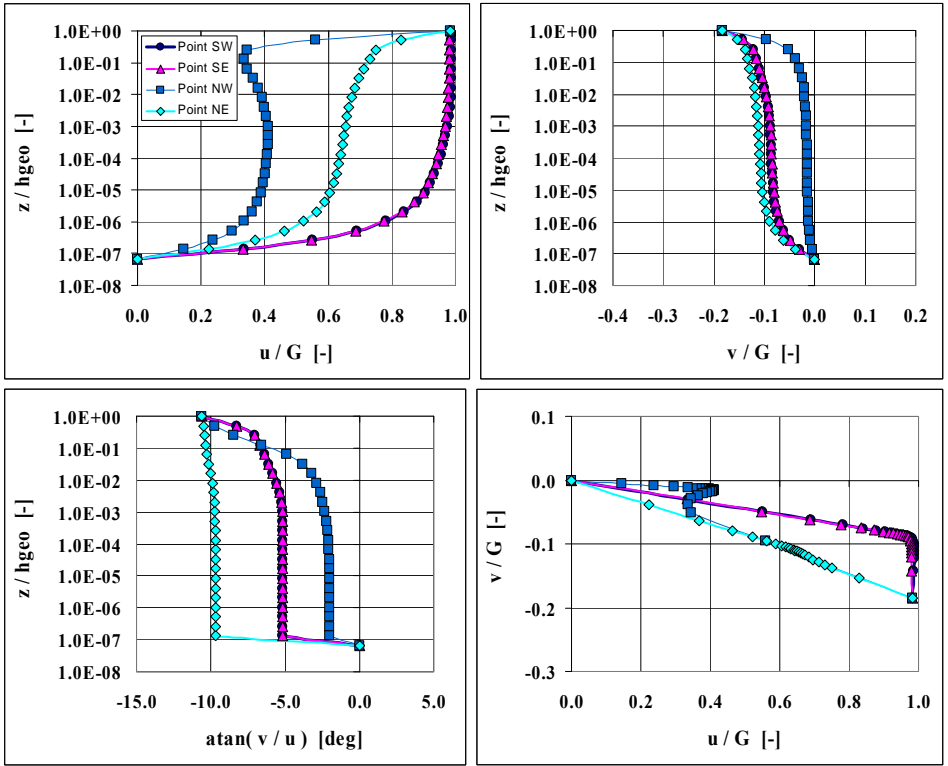


Figure 5.2 *Like figure 5.1 but for a geostrophic height of 1500 m*

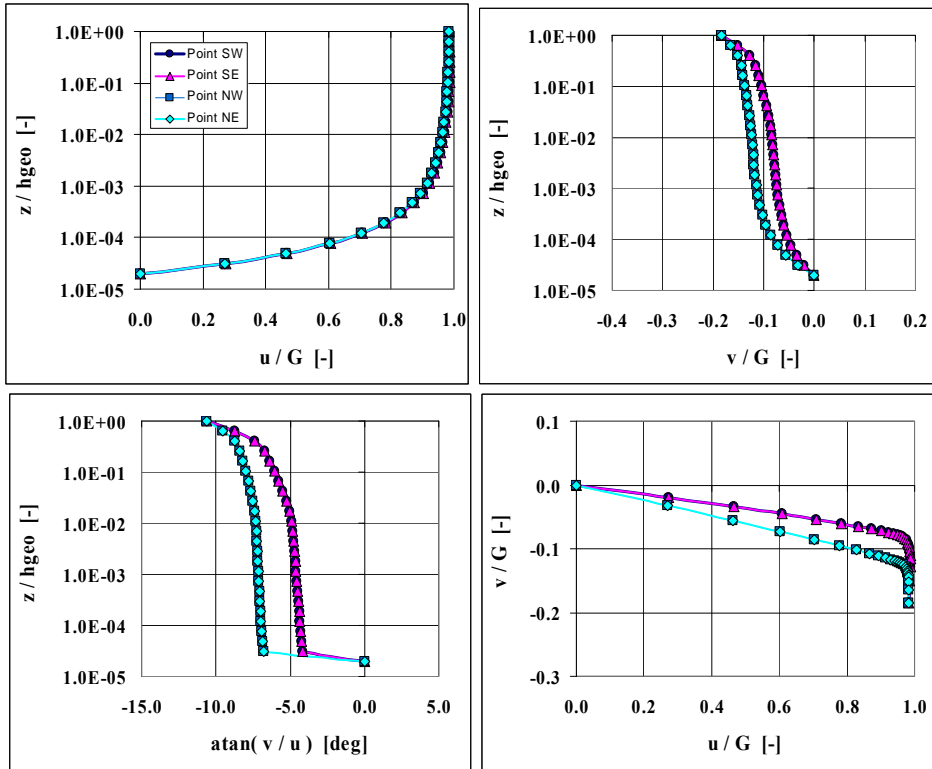


Figure 5.3 Like figure 5.1 but for a surface roughness length of 1 cm

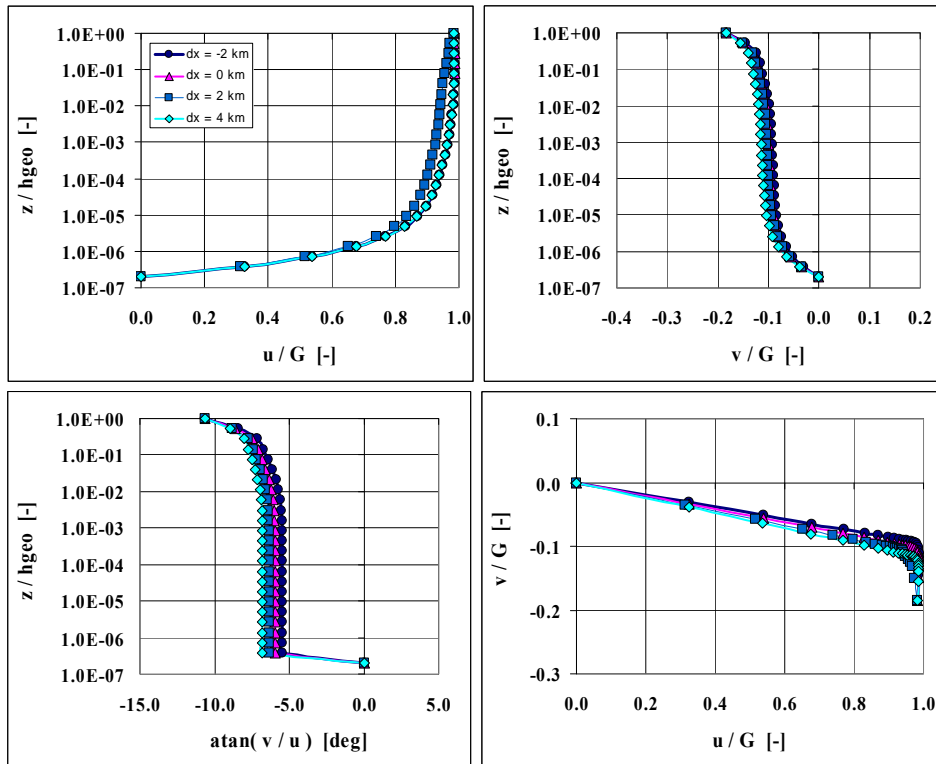


Figure 5.4 *Vertical profiles of streamwise velocity u and spanwise velocity v for different distances d_x behind a wind turbine as made non-dimensional with the geostrophic velocity G and the geostrophic height h_{geo} ; valid for a geostrophic height of 500 m and a surface roughness length of 0.1 mm*

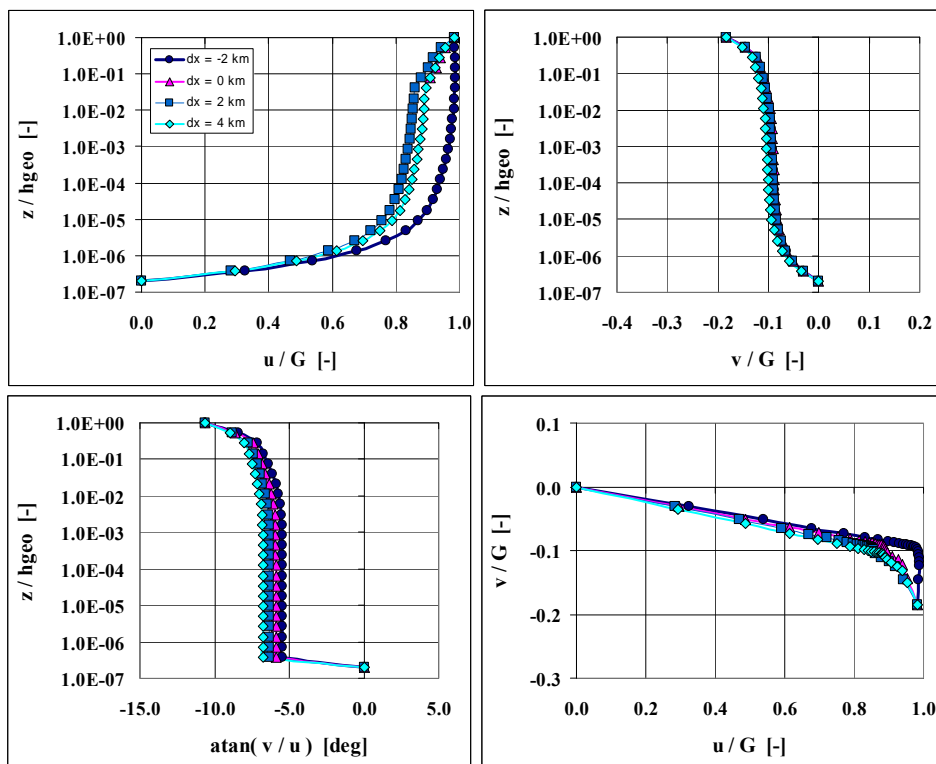


Figure 5.5 *Like figure 5.4 but for a wind farm*

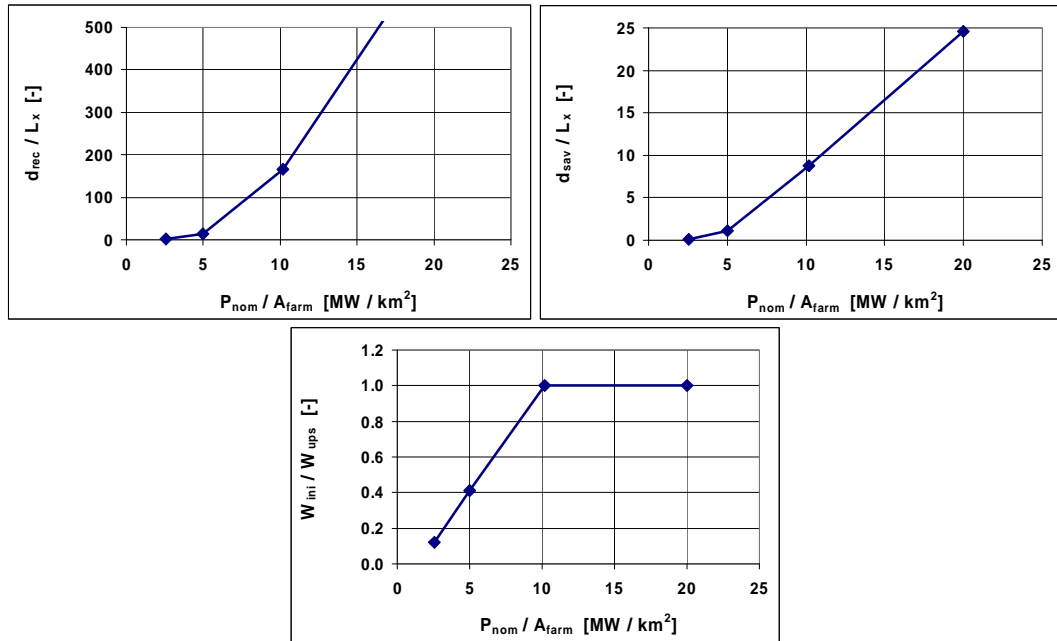


Figure 5.6 Impact of nominal power density P_{nom}/A_{farm} for a wind farm operating in a geostrophic velocity of 14 m/s on (a) the velocity recovery distance d_{rec} , (b) the minimum save distance d_{sav} and (c) the initial downstream velocity W_{ini} . Velocities are relative to the upstream velocity W_{ups} and whereas distances are relative to the streamwise wind farm length scale L_x . The geostrophic height is 500 m and the surface roughness length is 0.1 mm

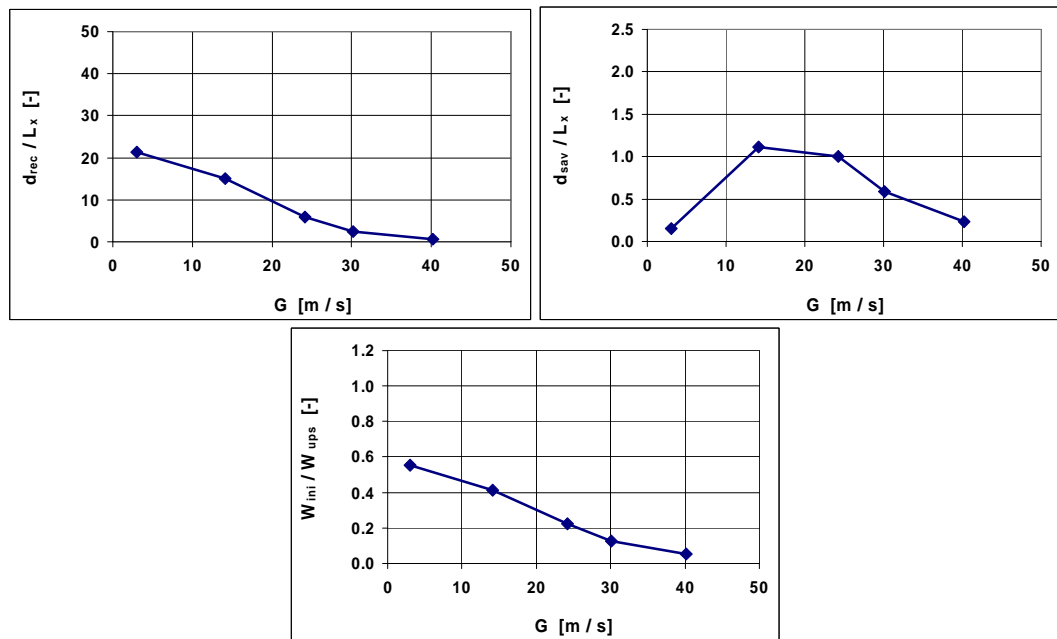


Figure 5.7 Impact of geostrophic velocity G on a wind farm with a nominal power density of 5 MW/km² on (a) the velocity recovery distance d_{rec} , (b) the minimum save distance d_{sav} and (c) the initial downstream velocity W_{ini} . Velocities are relative to the upstream velocity W_{ups} and whereas distances are relative to the streamwise wind farm length scale L_x . The geostrophic height is 500 m and the surface roughness length is 0.1 mm

5.3 Impact of wind farm design parameters and meteorological parameters

Wind farm design parameters include separation distance from and layout (spacing, nominal power density) of the wind farm, and hub height and rotor diameter of the wind turbine. The impact of nominal power density is studied by changing the turbine separation distance in the hypothetical wind farm between 5 and 14 times the rotor diameter and keeping the geostrophic velocity at a constant value such that the upstream hub-height velocity is halfway cut-in and nominal. Figure 5.6 shows that both the relative velocity recovery distance d_{rec}/L_x and the relative minimum save distance d_{sav}/L_x increase with the nominal power density, and that also the relative initial velocity deficit $(W_{ups}-W_{ini})/W_{ups}$ increases with the nominal power density from 6% (turbine separation 14 rotor diameters) to 100% (5 rotor diameters).

Meteorological parameters include geostrophic velocity, geostrophic height and surface roughness length. Figure 5.7 shows the impact of the geostrophic velocity for the hypothetical wind farm for hub height velocities near cut-in, halfway cut-in and nominal, near nominal, halfway between nominal and cut-out, and beyond cut-out. The relative velocity recovery distance is found to decrease with the geostrophic velocity, from a value of 20 at low geostrophic velocities to a limit value near 0 at high geostrophic velocities. The relative minimum save distance is found to have a maximum of the order of the streamwise wind farm length scale L_x , which is reached at geostrophic velocities between 15 m/s and 25 m/s. The relative initial velocity deficit $(W_{ups}-W_{ini})/W_{ups}$ is found to decrease with increasing geostrophic velocity, and the largest absolute initial velocity deficits $W_{ups}-W_{ini}$ (of in this case 6.3 m/s) occur when the hub-height velocity is near nominal.

6. Summary

In this report a new method has been presented for determining the interaction between a wind farm and the prevailing wind for wind energy siting studies. In addition first insights have been presented on the modification of the wind field due to a wind farm.

A code called MFwWF (Mesoscale Flow with Wind Farming) has been developed in order to calculate the effect of one wind farm on another wind farm while taking the entire planetary boundary layer into account. The code has been validated by using measured data from large offshore wind farms, and is available for application to other wind farms.

In chapter 3 it is shown that a neutral planetary boundary layer flow which interacts with wind farms essentially is steady and two-dimensional; and that the convective forces, the Coriolis forces and the vertical and spanwise gradients of the turbulent momentum fluxes all have the same order of magnitude. A numerical representation in the form of backward finite differences allows for an implicit solution of the two horizontal velocity components in vertical direction, iterating on the turbulent viscosity, in combination with a marching solution and a mass/energy conserving scheme in the horizontal directions. The continuity equation is satisfied by employing the Lagrange multiplier method to the velocity components that satisfy the continuity equation.

In chapter 4 the new method is validated by using measured wind speeds downstream of the Horns Rev wind farm and the Nysted wind farm. Resolved relative velocity deficits (point values which originate from the calculated grid cell averaged velocity deficits) come within 5% of the relative velocity deficits that have been measured.

In chapter 5 resolved profiles are presented which show how most of the wind speed change occurs in the lower part of the boundary layer and how most of the wind direction change occurs in the upper part. These profiles reveal that the thinner the boundary layer or the larger the surface roughness, the larger the wind direction change. Near a wind turbine with a rotor diameter of 100 m operating at a full load of 5 MW the velocity deficit is of the order of 5% of the upstream value, the wind direction change is increased with 1...2 deg, and the velocity recovery distance is of the order of 100 rotor diameters. For a wind farm with 22 of these turbines these numbers are 15%, 2...3 deg, and 2 wind farm length scales.

In addition in chapter 5 initial velocity deficits and velocity recovery distances are presented that show the impact of nominal power density and geostrophic velocity for a wind farm which consists of 22 wind turbines with a nominal power of 5 MW. The initial velocity deficit relative to the upstream velocity decreases with increasing geostrophic velocity in general, and ranges from 6% (at a turbine separation of 14 rotor diameters) to 100% (at a separation of 5 rotor diameters) if the velocity at hub height is halfway cut-in and nominal.) Both the relative velocity recovery distance and the relative minimum save distance increase with the nominal power density, and the relative initial velocity deficit increases with the nominal power density from 6% (at a turbine separation 14 rotor diameters) to 100% (at a turbine separation of 5 rotor diameters). The relative velocity recovery distance decreases with the geostrophic velocity, from a value of 20 at low geostrophic velocities to a limit value near 0 at high geostrophic velocities, and the relative minimum save distance reaches a maximum value of the order of the streamwise wind farm length scale (which maximum is reached at geostrophic velocities between 15 m/s and 25 m/s). Finally, the relative initial velocity deficit decreases with increasing geostrophic velocity, and the largest absolute initial velocity deficits (of in this case 6.3 m/s) occur when the hub-height velocity is near nominal.

References

- S. Baidya Roy et al., 2004, *Can large wind farms affect local meteorology?* J. Geoph. Research, Vol. 109, D19101
- R. Barthelmie et al., 2003, *Efficient Development of Offshore Windfarms (ENDOW)*, Report Risø-R-1407(EN)
- M.B. Christiansen and C.B. Hasager, 2005, *Wake studies around a large offshore wind farm using satellite and airborne SAR*, In: 31st Int. Symp on Remote Sensing of Environment, St Petersburg, Russian Federation
- C. Dyrbye and S.O. Hansen, 1997, *Wind Loads on structures*, John Wiley and Sons
- D.L. Elliott, 1991, *Status of wake and array loss research*, In: Proc. Windpower91, Palm Springs, California, 24-27 September 1991
- J.H. Ferziger and M. Perić, 1997, *Computational methods for fluid dynamics (2nd ed.)*, Springer
- S. Frandsen et al., 2004, *The necessary distance between large wind farms offshore - Study*, Risø National Laboratory, Report Risø-R-1518(EN)
- J.R. Garratt, 1994, *The atmospheric boundary layer*, Cambridge University Press
- T. Hegberg and P.J. Eecen, 2002, *The effect of large wind farms on the atmospheric boundary layer*, In: Proc. Global Wind Power Conference 2002, Paris, France
- T. Hegberg, G.P. Corten and P.J. Eecen, 2004, *Turbine interaction in large offshore wind farms - Atmospheric boundary layer above a wind farm*, Report ECN-C--04-033
- J.R. Holton, 1992, *An Introduction to dynamic meteorology (3rd ed.)* Academic Press
- M-K Liu et al., 1983, *Mathematical model for the analysis of wind-turbine wakes*, J. Energy, Vol. 7, No. 1, pp. 73-78
- D.J. Milborrow, 1980, *The performance of arrays of wind turbines*, J. Industrial Aerodynamics, 5 (1980), pp. 403-430
- J. Nikuradse, 1932, *Gesetzmässigkeit der turbulenten Strömung in glatten Rohren*, Forschg. Arb. Ing.-Wes No 356
- P. Rooijmans, 2004, *Impact of a large-scale offshore wind farm on meteorology - Numerical simulations with a mesoscale circulation model*, Universiteit Utrecht, Masters thesis
- H. Schlichting, 1979, *Boundary layer theory (7th ed.)*, McGraw-Hill Book Company
- H. Tennekes and J.L. Lumley, 1972, *A first course in turbulence*, The MIT Press
- D.C. Willcox, 1998, *Turbulence modelling for CFD (2nd ed.)*, DCW Industries Inc.